AD-A166 888 QUATERNARY NARROW-BAND SEMICONDUCTORS (HGTE)X(INSB)1-X 1/2
FOR FAR-INFRARED DETECTORS(U) SAN DIEGO STATE UNIV
FOUNDATION CA L I BERGER 31 AUG 86 N00014-83-K-0588
UNCLASSIFIED F/G 17/5 NL

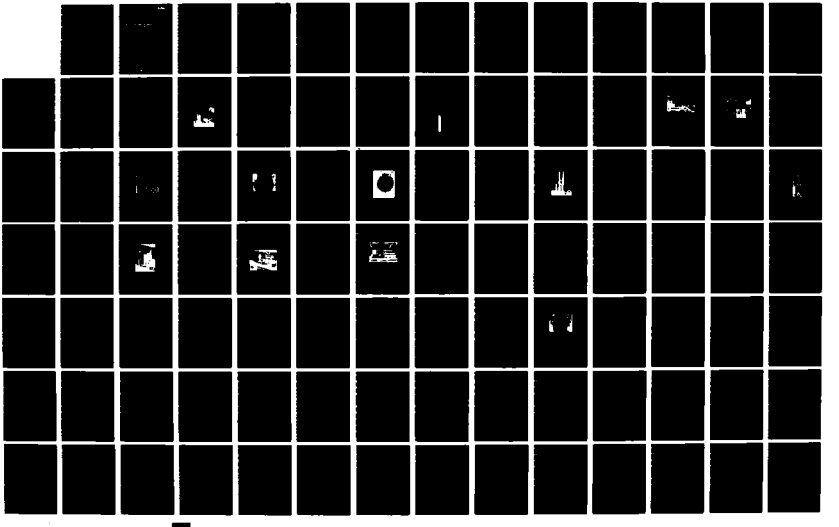

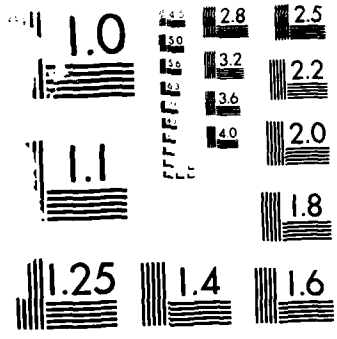

MICROCOPY RESOLUTION TEST CHART

STANDARDS 1963 A

SDSU FOUNDATION

12

Quaternary Narrow-band Semiconductors

$(HgTe)_x(InSb)_{1-x}$ for Far-infrared Detectors

Submitted to
Office of Naval Research
by
San Diego State University Foundation

ANNUAL REPORT

PROJECT TITLE: QUATERNARY NARROW-BAND SEMICONDUCTORS $(HgTe)_x(InSb)_{1-x}$ FOR FAR-INFRARED DETECTORS

GRANT NO: N00014-83-K-0588

PRINCIPAL INVESTIGATOR: LEV I. BERGER
DEPARTMENT OF PHYSICS
San Diego State University
(619) 265-6163/6240

SUBMITTED TO: OFFICE OF NAVAL RESEARCH
ARLINGTON, VIRGINIA 22217

STARTING DATE: SEPTEMBER 1, 1983

REPORTING PERIOD: SEPTEMBER 1, 1984-AUGUST 31, 1985

COMPLETION DATE: AUGUST 31, 1986

Lev I. Berger

LEV I. BERGER
PRINCIPAL INVESTIGATOR

Table of Contents

ABSTRACT

This annual report includes a description of results from work on an investigation of the quaternary system $(HgTe)_x(InSb)_{1-x}$ in accordance with Project N00014-83-K-0588 during the second year, from September 1, 1984 to August 31, 1985.

In the course of this time period, the systems for Bridgman-Stockbarger growth, hot-wall epitaxial growth, and isothermal epitaxial growth were designed, assembled, and tested. On the basis of the resutls of the testing stage, the temperature-pressure-time regimes for single-crystal and epitaxial layer growth were developed. Several single crystals of the solid solutions of HgTe in InSb with the HgTe contents up to 15 mole percent were grown and assessed. The report includes growth parameters for the bulk crystals with composition x = 0.05, 0.10, 0.12 and 0.15. These crystals cover the energy gap range from 0.10 to 0.14 eV or the cut-off wavelength range from 12.4 to 8.9 μm.

The synthesized single crystals and epilayers were used for microstructure analysis, microhardness measurements and X-ray analysis. It has been established that the single crystals grow predominantly in the [111] direction and possess relatively high axial and radial uniformity. The axial size of the grown single crystals was up to 80 mm with a 10 mm diameter. The electrical transport parameters were evaluated from the results of electrical conductivity and Hall constant measurements. As usually takes place, carrier

mobility of the bulk crystals is greater than that of the epilayers. The magnitudes of mobility of the grown crystals were of the order of 10^5 $cm^2/V \cdot sec$ at room temperature; whereas, for the films this parameter did not exceed 10^3 $cm^2/V \cdot sec$. The temperature dependence of the transport parameters suggests that the electron mobility is limited mainly by acoustic phonons.

The investigation of the optical parameters consisted of transmittance, reflectance, and photoconductivity measurements. The results were used for evaluation of the fundamental optical absorption edge as a function of the sample composition. The photoconductivity data demonstrated that the alloys had a relatively long excess carrier lifetime at low thermal equilibrium carrier concentration and high quantum efficiency. It is reasonable to conclude that the investigated single crystalline samples satisfy the basic requirements for high photoconductive responsivity.

In the process of preparation for the crystal growth, and in connection with the plans for the third year of work, the thermal conductivity of the alloys as a function of composition was measured at room temperature.

The results of the first two years of work with this Project give us reason to conclude that the investigated group of semiconductor materials evidently possesses properties which can be successfully used for manufacturing infrared detectors of a new class.

The basic steps of the third year of work are (a) correction of methods of single crystal and thin film preparation, (b) design and manufacturing of the models of photoconductive and photovoltaic detectors on the basis of $(HgTe)_x(InSb)_{1-x}$ alloys, and (c) investigation of the detection parameters, such as minimum detectable power, signal-to-noise ratio, specific detectivity, and their dependence upon the detected radiation frequency, temperature, etc. The main purpose of this project is the development of growth technique for crystals and epitaxial layers of $(HgTe)_x(InSb)_{1-x}$. The goal is to synthesize and evaluate single crystals and/or epitaxial films of these substances and provide comprehensive recommendations for their effective use as materials for far-infrared photoresistive and/or photovoltaic detectors.

1. INTRODUCTION

This report includes results of the second year investigation of the semiconducting alloys in the quaternary (pseudo-binary) system HgTe-InSb.

During the first year of work on this Project, it was shown that solid solutions in the $(HgTe)_x(InSb)_{1-x}$ section of the pseudo-quaternary system $InSb-In_2Te_3-HgTe-Hg_3Sb_2$ exist at least in the limits of $0 \leq x \leq 0.2$. In these limits the optical energy gap is changing linearly from 0.17 eV to 0.086 eV (from 7.3 μm) with the rate 4.2 meV/percent of HgTe, which is much less than that of the HgCdTe system (19 meV/percent of HgTe).

The experiments showed that synthesis of single-phase semiconducting ingots took place at relatively low temperatures, and the amount of successful cycles of synthesis was greater than 90% of all the total amount of cycles. This is much better than in the case of HgCdTe where this parameter is smaller than 60%. The reason for it is partially due to much lower synthesis temperatures for $(HgTe)_x(TnSb)_{1-x}$ in comparison with that of HgCdTe and correspondingly lower vapour pressure.

Our investigation has shown that at $x > 0.20$ the process of homogenization of alloys is slowed down and takes the time period of not less than 180 days. On the other hand, the materials with $x > 0.20$ in accordance with the theoretical predictions are more of a metallic nature than the semiconductor one, and do not represent a substantial interest as materials for infrared detection. Taking it

into consideration, we concentrated our attention upon the single-phase alloys with x in the limits from 0.0 to 0.20.

It was shown that the alloys have a crystal lattice of the $F\bar{4}3M$ type and the lattice parameter obeys Vegard's law. The microhardness of the alloys is much greater than those of HgCdTe (cf. for example, 210 and 45 kgp/mm^2 perspectively) and even on the first steps of our experiments we had had an advantage because of it, having a smaller amount of broken samples in the process of mechanical treatment (cutting, polishing, etc.).

Electrical conductivity and Hall effect measurements had been used to characterize the transport properties. All samples possessed conductivity of n-type. This contrasts with the alloys of HgCdTe and may be explained if we assume that probable losses of the mercury atoms from the surface of an ingot do not change electrical properties substantially, because in the InSb alloys, that have a relatively small amount of HgTe, second members of rhs of expressions for electrical conductivity, σ, and Hall constant R_H [13]:

$$\sigma = |e|\,\mu_p\,p + |e|\,\mu_n\,n \tag{1.1}$$

$$R_H = \frac{r_H\mu_p^2 p}{|e|(p\mu_p + n\mu_n)^2} - \frac{r_H\mu_n^2 n}{|e|(p\mu_p + n\mu_n)^2} \tag{1.2}$$

are usually much greater than the first ones. This is partially connected to the fact that mobility of electrons, μ_n, in the InSb alloys is much greater than that for holes, μ_p. In our

experiments, parameter $|N_D-N_A|$ was changing synbatically with x and had an order of magnitude 10^{16} - 10^{18} cm^{-3} which is typical for the polycrystalline samples of alloys on the basis of InSb, as well as the magnitude of the product σR_H, that was about 4 x 10^4 $cm^2/V \cdot sec$.

Optical measurements on the polycrystalline samples, which included both transmittance and reflectance experiments, demonstrated practically linear decrease of the energy gap with the HgTe concentration increase. The results of the optical measurements had a reasonable agreement with the electrical and galvano-magnetic data.

The results of our experiments during the first project year had given us reason to conclude that the investigated alloys might be considered as a very promising and prospective material for far-infrared detectors as well as one for some other semiconductor devices.

As it is well known, reliable and reproduceable data of the material parameters can be obtained only on the basis of the results of the measurements of the parameters on single crystalline samples of the material investigated. Furthermore, the ability of growth of bulk single crystals and/or thin epitaxial layers is almost always an unavoidable step in the process of introduction of a new material in the semiconductor industry. The problem of single crystals was the main part of the second year experiments.

The reported year schedule included: (a) bulk crystal growth and epitaxial thin film growth which were preceeded by a detailed

investigation of the process of homogenization of the polycrystalline ingots used for growth; (b) the Laue and Debye-Scherrer x-ray analysis of the grown crystals and films; (c) detailed investigation of their parameters; electrical conductivity, Hall constant, optical absorption and reflectance, photoconductivity, as well as (d) microhardness and thermal conductivity.

The main objective of the second year program is to collect all necessary data regarding the new intrinsic semiconductor material that will be used in our third year work to manufacture and investigate the models of a new class of far-infrared detectors which, on the basis of our preliminary conclusions, shall have certain advantages in comparison with some existing detectors, and in particular, mercury-cadmium-telluride ones.

2. EXPERIMENTS

2.1. SINGLE CRYSTAL GROWTH

In the Bridgman-Stockbarger crystal growth, an alloy is contained in a fused-silica ampule. The ampule carries a significant part of the heat during the solidification process. On the other hand, thermal conductivity of the alloy in liquid and solid states as well as the difference in their composition will also play an important role in removal of the latent heat of solidification from the melt-crystal interface. These factors will determine the shape of the interface which, as was shown in Refs. [1-4], plays an important role in the compositional uniformity and defectiveness of the growing crystal. The shape of the interface is determined mainly by the radial temperature gradient in the melt and in the crystal near the interface. The commonly observed interface is a concave one upon which the growth takes place under neither isothermal nor isocompositional conditions.

To get a nearly flat interface, we designed a Bridgman-Stockbarger growth system with an inner diameter only slightly greater than that of the growth ampule. The system consisted of three sections: an alloying section, a growth section, and an annealing section. The schematic arrangement of the parts is presented in Figure 1. Initially, the ampule with the mixture of HgTe and InSb in a proper ratio was inserted in the upper tube furnace A. This step of the process was designed to make a homogeneous liquid alloy InSb-HgTe. In part of our experiments we applied the vibrational mixing of the alloy to accelerate the process of

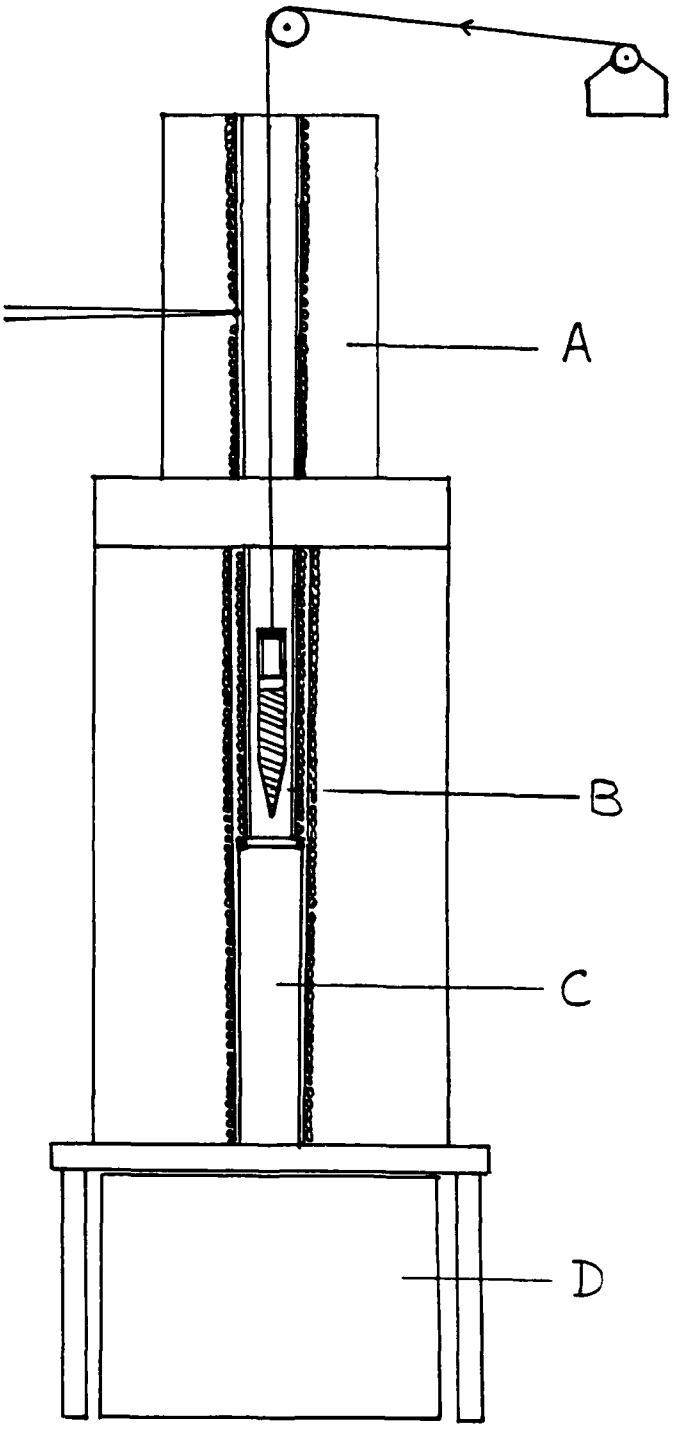

Figure 1(a). The Bridgman-Stockbarger furnace cross section.

homogenization (oscillation frequency 120Hz). At the end of this step of the process, the ampule with the alloy was lowered to the furnace B. Both furnaces had copper (or brass) cylinders inside of them to provide uniform temperature. The temperatures in the furnaces B and C were chosen to yield a nearly flat interface shape. The theoretical reason for the choice was based upon the assumptions that (a) the main part of heat is transported in the furnace by radiation, (b) the ampule material (fused silica) is transparent for visible and infrared radiation at $\lambda < 4$ μm and (c) the emissivities, ε, of all heated parts are equal to each other.

To have a nearly flat crystallization front we have to satisfy the equilibrium condition

$$\varepsilon_u \sigma T_u^4 - \varepsilon_u \sigma T_u = \varepsilon_s \sigma T_s^4 - \varepsilon_l \sigma T_l^4 \qquad (2.1.1)$$

where σ is the Stefan-Boltzmann constant and the subscipts u, s, and l relate to the upper (hotter) part, interface, and the lower (cooler) part of the system respectively.

From (2.1.1) we get

$$T_l = (2T_s^4 - T^4)_u^{1/4} \qquad (2.1.2)$$

Temperature T_u usually is chosen to be a few degrees above the liquidus to avoid the constitutional supercooling.

After completion of the process of preparation of a homogeneous liquid alloy, the ampule started to move down with a chosen velocity. The choice of the speed was constrained by the requirement to

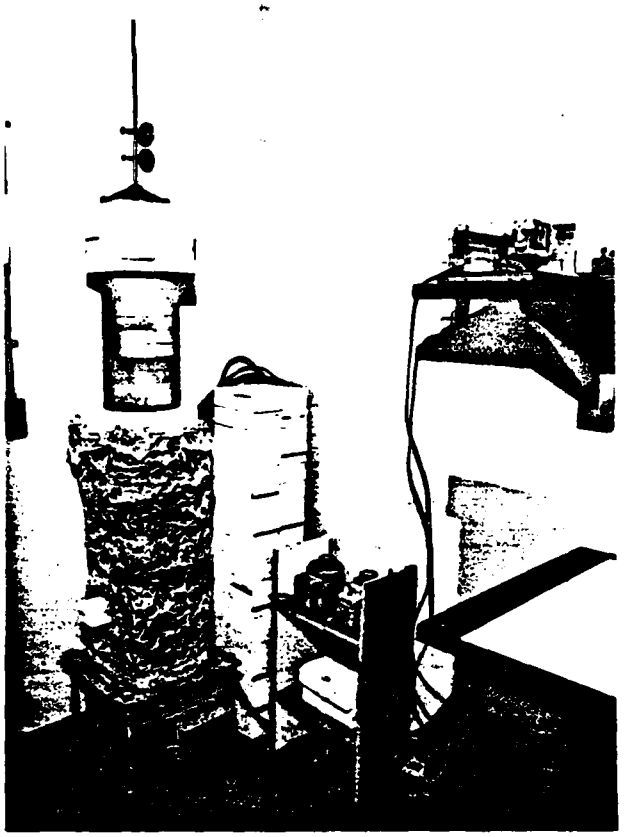

Figure 1(b). The general view of the Bridgman-Stockbarger growth unit.

avoid constitutional supercooling as well as to prevent segregation of HgTe with respect to InSb, due to the separation of the liquidus and solidus lines.

Tiller [5] gave the formula for the velocity, v_o, above which constitutional supercooling becomes significant:

$$v_o = GDk/C(1-k)m \ , \qquad (2.1.3)$$

where G is the temperature gradient in the melt, D the diffusion coefficient in the melt, k the segregation coefficient, C the concentration of solute in the solid, and m the liquidus slope.

In our search for the temperature and velocity magnitudes we used the phase diagram of pseudo-binary system InSb-HgTe [6]. In our investigations, we studied the effect of various treatments of the inner surface of the growth ampule, including carbon coating, flaming, etc. It was evident that the best results took place with the routinely purified silica. From our point of view, the most important parameter that determines the success of the Bridgman-Stockbarger growth is uniformity of transparency of the crucible walls for the (infrared) radiation. The same effects were discovered by Bartlett et al. [7] while investigating growth of the $Cd_xHg_{1-x}Te$ crystals.

The mechanical driving unit used in the experiments was able to drive an ampule at a speed between 0.01 to 4.0 cm/hr. Quartz ampules with the inner diameter of 10.0 mm and the outer diameter of 14.3 mm were used for crystal growth. The thickness of the ampule

walls was chosen only to satisfy the requirements of the Health and Safety Department. Our synthesis and crystal growth laboratory is located in a classroom and office building of SDSU.

The inner surface of the ampule was ground with 0.05 micro powder of gamma alumina to clean the surface of silica from a microscopic layer of glass, carbon, and other mechanical precipitates. After the mechanical cleaning, the ampule was washed in deionized water (DW) and filled with a saturated solution of KOH and methanol. After 24 hours, the ampule was rinsed again in DW, and filled with a mixture of HNO_3 and HCl (1:3 by volume). After 24 hours, the ampule was rinsed thoroughly with DW (ten cycles, 10 minutes each) and after this was evacuated with a diffusion pump unit to 10^{-4} torr. The evacuated ampule while pumping was heated to 900°C in the part of it which was intended to hold the load. After baking, the ampule was cooled, disconnected from the vacuum system, and loaded with the chosen amount of binary components. A thoroughly cleaned silica rod with a diameter only slightly smaller than that of the ampule inner diameter was then inserted in the ampule. The latter was connected to the diffusion pump, evacuated, and sealed off.

In our estimations of (a) the temperatures in the different parts of the Bridgman-Stockbarger furnace, (b) speed of the ampules, and (c) the lengths of the load, we used magnitude of thermal conductivity of fused silica κ = 14.8 mW/cm·K [8], magnitudes of κ for $(HgTe)_x(InSb)_{1-x}$ alloys from our measurements (see section 3.6 of this Report), and magnitudes of InSb density in solid state D_S(480°C) =

5.77 g/cm^3 and in liquid state D_L(550°C) = 6.43 g/cm^3 after Glazov et al. [9]. A photo of a loaded and sealed ampule is presented in Fig. 2. See Appendix 1 for the preparation furnace dimensions.

2.2. THIN FILM GROWTH BY VAPOR-PHASE EPITAXY

In our experiments with epitaxial layer growth we used two methods: (1) the hot-wall epitaxy HWE [10] and (2) the evaporation-diffusion under isothermal conditions, EDRI [11, 15, 16].

The main advantage of the HWE technique is in its relative simplicity and the possibility to grow epitaxial layers under conditions closer to thermodynamic equilibrium than most other evaporation methods [12]. The system consists essentially of a heated silica tube with two independent furnaces, one of which evaporates the source material (e.g., HgTe) and serves also to direct the evaporating particles from the source to the substrate. The other heater keeps the substrate at a chosen deposition-diffusion temperature. The substrate at the top closes the tube. In this design, loss of material is less and a clean environment is kept inside the tube.

The apparatus (Fig. 3) consists of the ceramic pedestal, 1, that holds a flat-bottom quarts ampule, 2, with a heater on the outer surface, 3, and a special aperture in the bottom to hold a thermocouple, 4. The ampule upper edge is held by a ceramic ring, 5, and the latter is connected to the assembly column, 6. The ring, 5, has a horizontal slit in it just above the upper edge of the

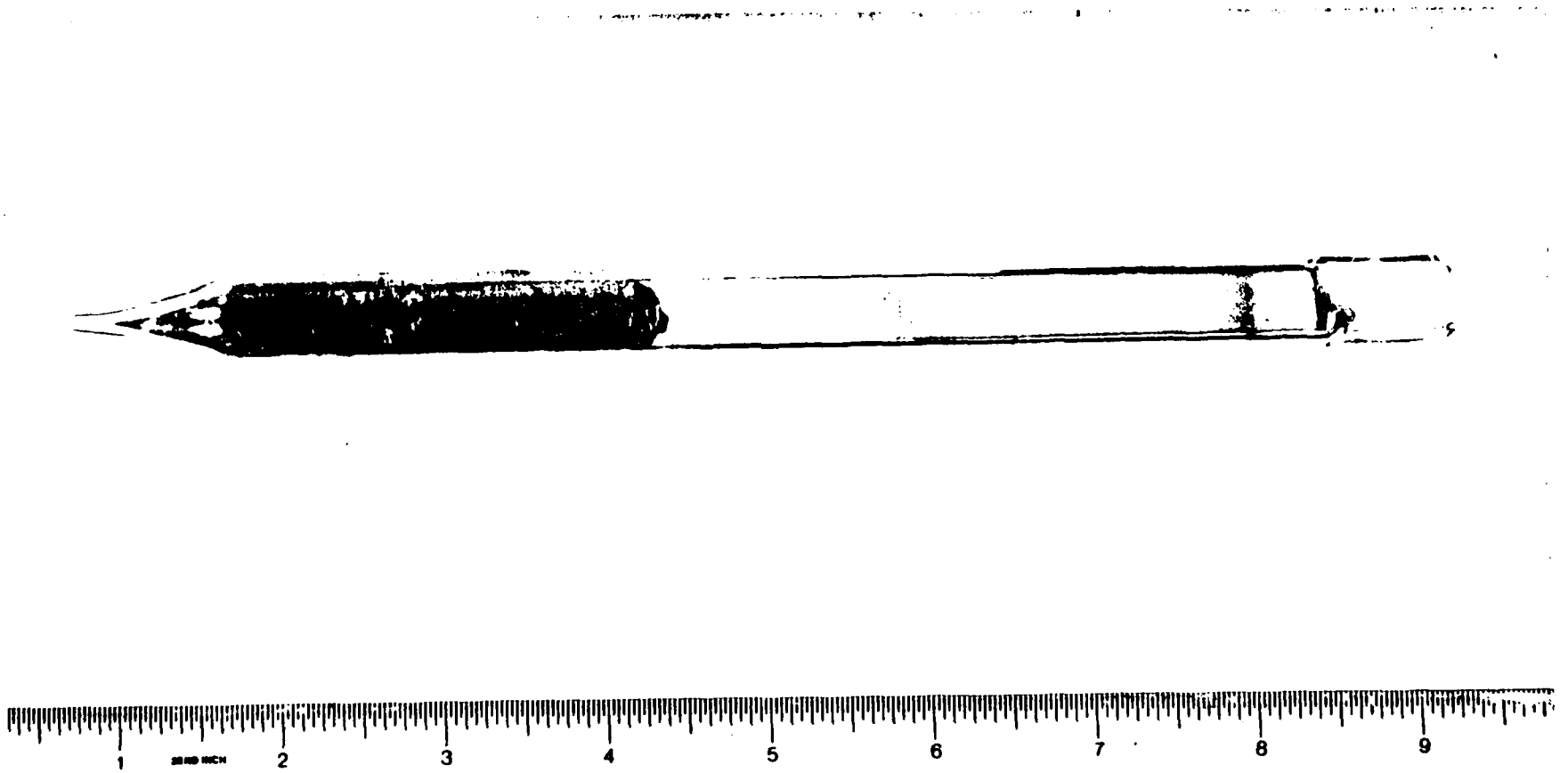

Figure 2. An ampule for crystals growth after the process.

ampule, 2. The slit is a part of a shutter system that may separate the source of depositing material and the substrate, 7. The other part of the shutter system is a flat stainless-steel shutter, 8, with a round opening in it. Diameter of the opening is equal to that of the ampule 2. The shutter is connected to a magnet, 9, that is located in an appendix, 10, on the surface of a vacuum bell, 11. The substrate, 7, reposes on a polished quartz ring, 12, which lies on the ring 5. The substrate, 7, holds another flat-bottom quartz ampule, 13, that serves as a substrate heater. This heater consists of two coaxial ampules, one of which, 14, has a flat bottom and the other one, 15, has a narrow extension at the bottom. The outer diameter of the ampule, 15, is only slightly smaller than the inner diameter of the ampule 14. The ampule 14 was partially filled with tin shot, the ampule 15 was inserted in the ampule 14 almost to the bottom of it, and then the system was evacuated and sealed. The electric heater, 16, is wound around the surface of the ampule, 14. The tin inside of the heater serves to create uniformity and stability of the substrate temperature provided by high thermal conductivity of the tin melt. The temperature is measured by the thermocouple, 17. The evaporation-deposition system was surrounded by a reflecting stainless-steel screen (not shown on Figure 3) and connected to a diffusion vacuum pump system (see Figure 4).

Our preliminary experiments had shown that nonuniformity of radial temperature distribution on the deposition side of the InSb

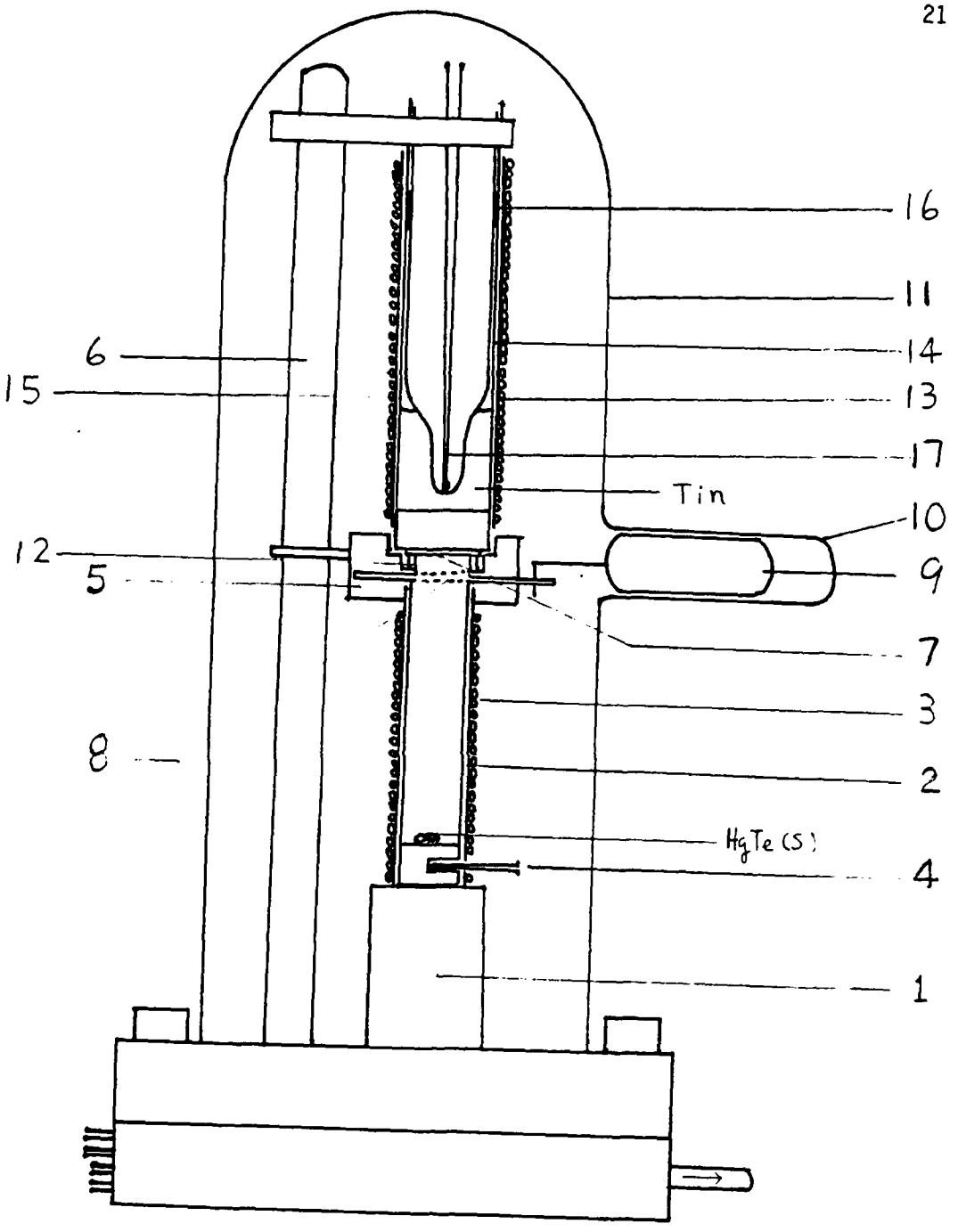

Figure 3. The experimental arrangement used for the hot-wall epitaxy.

substrates was below the level of sensitivity of the temperature measuring device ($\Delta T_{sens} = 10^{-1}K$).

The epitaxial growth by the EDRI method was done on the single crystalline InSb substrates with the HgTe powder as a source. The geometry of the growth system was similar to one used by Tufte and Stelzer [14] for HgCdTe epitaxy. The source of the evaporated material was HgTe 99.999%. The substrate in the shape of a disk 10 mm in diameter was cut from a single crystal with the disc cutter SBT Inc., Model 350 (Figure 5), and thoroughly etched and washed prior to experiment. A quartz ring, 1, Figure 6, was inserted on the bottom of a flat-bottom quartz ampule. After it, a definite amount of the HgTe powder, 2, was loaded inside the ring. The amount of HgTe was chosen on the basis of desirable magnitude of x in the $(HgTe)_x(InSb)_{1-x}$ layer. The InSb substrate, 3, of (111) orientation, 1-mm thick, was placed on the ring. The inner diameter of the ampule was only slightly greater than that of the InSb substrate. After it a quartz rod, 4, was inserted in the ampule, the latter was connected to the vacuum system, evacuated and sealed out.

The thickness of the rirg, 1, was equal to 5 mm which was equal to that in [14], but much greater than in [15, 16]. We believe that in our experiment greater distance is better from the point of view of uniformity of the vapor phase composition near the surface of substrate. On the other hand, evaporation of the atoms of the substrate in our case is negligibly small and is insignificant in the process of epitaxial growth, because of a substantial difference in

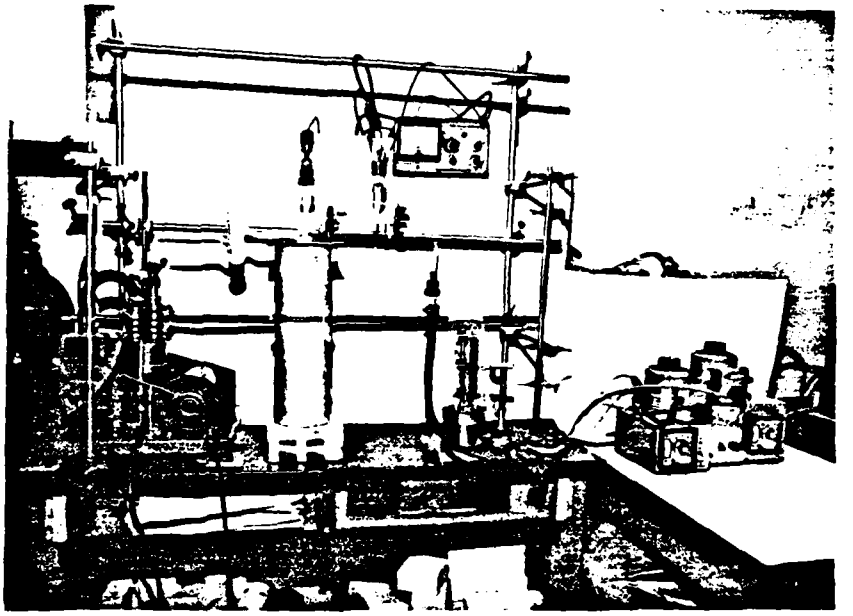

Figure 4. A general view of the apparatus for the hot-wall epitaxy.

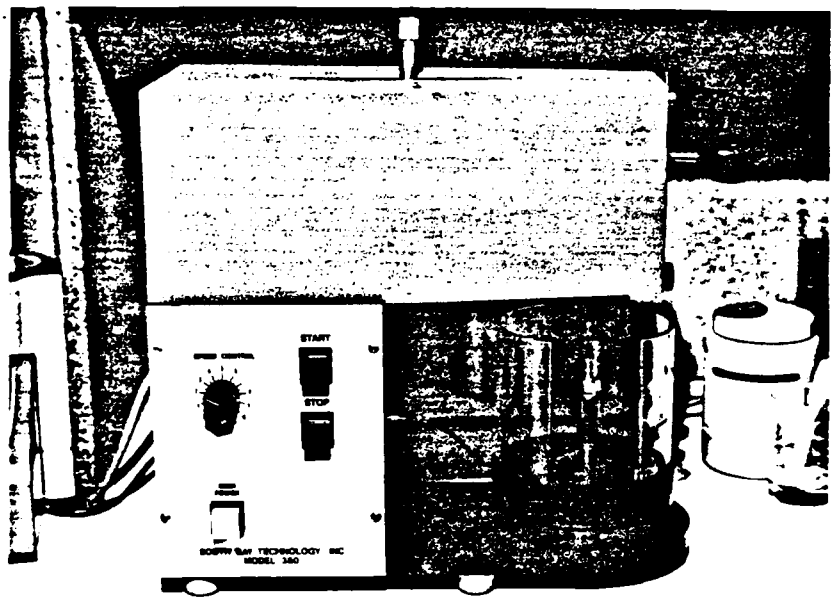

Figure 5. The crystal circular cutter SBI, Inc., Model 350.

the vapor pressure of Hg and Te in comparison with In and Sb. We believe that unsuccessful attempts by Marfaing et al. [11] to grow InSb on the CdTe and InAs substrate has its explanation not in the nonexistence of a mutual solubility between the corresponding materials (there is unlimited solubility in the InSb-InAs system [17]), but in the extremely low volatility of In and Sb in comparison with Cd, Te, and As. For the geometry of the epitaxial growth equipment, see Appendix 1.

2.3. MICROSTRUCTURE ANALYSIS AND MICROHARDNESS MEASUREMENT

Microstructure analysis of the polycrystalline specimens that were used in a part of the Bridgman-Stockbarger growth experiments was conducted according to a common routine which consists of a specimen being molded into an Epo-Kwick epoxy resin cylinder, the cylinder then was cut perpendicular to its axis in a chosen position, the open cut of the specimen was polished mechanically with 0.05 micro-powder of gamma alumina, the polished surface was etched in 1 to 2 dilution of 2:1:1 parts of concentrated HNO_3, HF, and HAC, respectively. In the majority of the synthesis cycles, the processes of the alloy homogenization in the liquid state was an initial part of the crystal growth. Microstrucure analysis of the grown and annealed crystals consisted of determination of the single crystal size, and the search for the existence of microscopically detectable defects and mosaic structure.

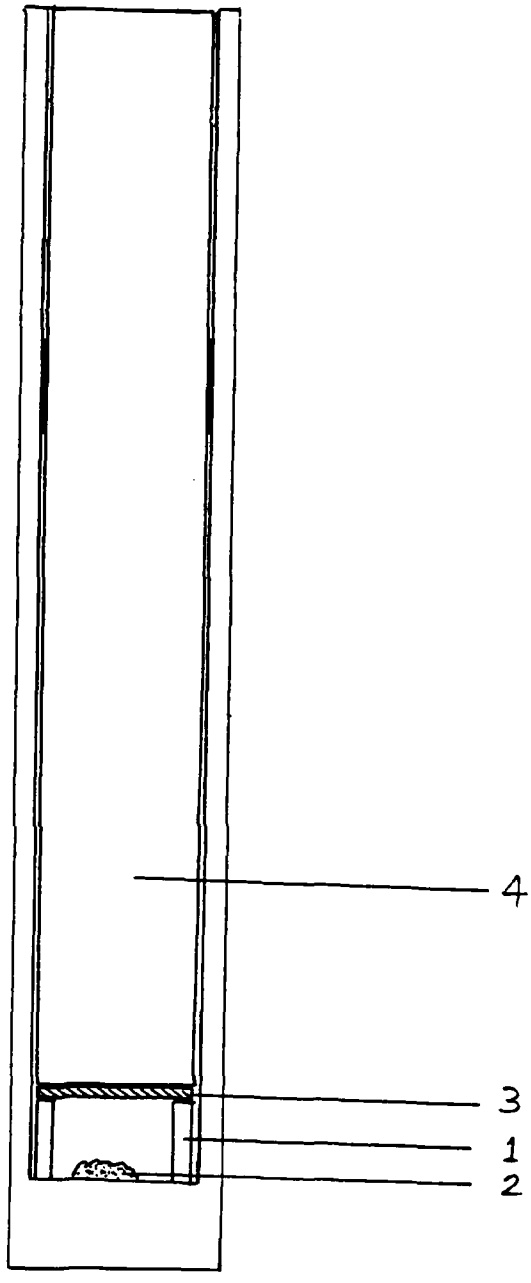

Figure 6. Experimental arrangement used for the EDRI epitaxial growth.

For this purpose we cut the ampule with the grown crystal on cylindrical portions, polished them mechanically, etched, and investigated the structure of their surface. It makes sense to mention again that we did not have difficulties with cutting ampules with single crystals inside because of the relatively high microhardness of the grown crystals in comparison with HgCdTe.

Microstructure analysis of the thin films of HgTe on the surface of InSb was conducted on the as-grown films with the different time-temperature regimes of the film deposition. Two typical photos of the initial stages of the epitaxial growth are presented in Figures 7 and 8. It is clear that at the lower rate of growth, centers of crystallization are uniform and have a definite orientation on the substrate. One can also see irregularities in the orientation of the centers of crystallization at the elevated rate of deposition. From our point of view, in accordance with the results of Varlamov et al. [18], who investigated preparation of CdTe layers on the InSb substrate, the difference may be explained by a finite rate of reaction between the deposited atoms and the substate. If the deposition rate is small, the deposited substance reacted chemically with the substrate and created the regular centers of crystallization following by the uniform epitaxial growth. At the higher rates, clusters of Hg atoms on the surface may create liquid centers (e.g., amalgams) with the substrate material, following chemical interaction with the substrate. In this case, at a certain degree of saturation, the liquid centers start to crystallize creating

Figure 7. Initial stage of the epitaxial growth of HgTe on the (111) InSb substrate by the EDRI. The average rate of growth was about 2 nm/sec. 450^{X}.

irregularities in the picture of the growing layer. The successfully grown epitaxial layers have a very uniform mirror-like surface similar to the surface of the initial substrate. Film growth was conducted at temperatures from 373K to 773K.

It is known ([17], p. 11), that microhardness, H, of a solid solution is very sensitive to its composition and defectiveness. In our experiments, we used the measurements of H to check the uniformity of single crystals and their orientation. The latter was used as an axiliary method to the Laue X-ray analysis. In many III-V crystals and their solid solutions it has been established [19-24] that H depends upon orientation of a surface tested relatively to the crystallographic directions. For example, in the case of InP, change of the angle by some 40° may change H from 370 to 410 Kgp/mm [24]. In our experiments, we have measured H across a polished and etched surface of a grown single crystal or an epilayer along two mutually perpendicular directions. For the epilayers, H also gives information regarding the layer thickness distribution. For the microhardness measurements we used a Leitz Microhardness Meter, Wetzlar, Germany. In our experiments the load 0.05 kgp was used. The experimental error in the measurements of H, calculated on the basis of the partial derivative method was equal to 2.5% without taking into consideration the ambient temperature fluctuations.

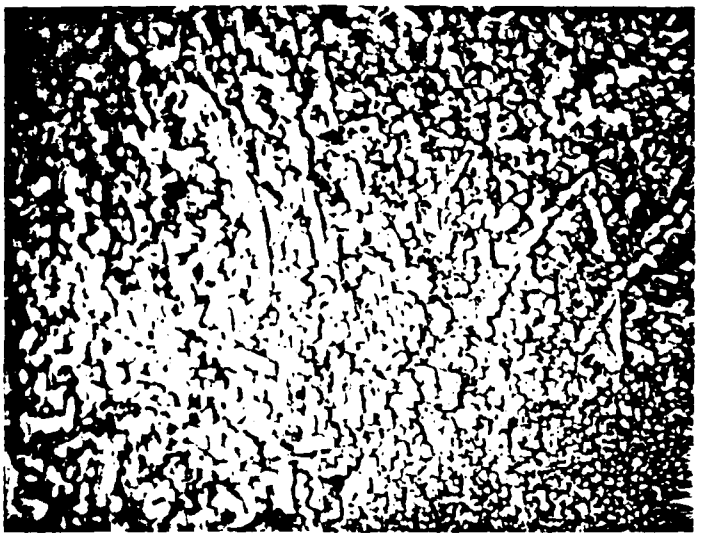

Figure 8. Initial stage of the EDRI process at the rate 5 nm/sec. 450^{X}.

2.4. X-RAY ANALYSIS

X-ray analysis was performed on the computer equipped X-ray diffractometer DIM 1057, Diane Corporation. Both the Laue and Debye-Scherrer methods were used. In spite of relatively small differences in the magnitudes of the lattice constants of the binary constituents (6.4623A for HgTe and 6.470A for InSb), the Debye-Scherrer experiments on the grown crystals have convinced us that in the system $(HgTe)_x(InSb)_{1-x}$ the axial compositional variation during Bridgman-Stockbarger-type directional solidification does not play such a substantial role as it does in the system HgCdTe.

The Laue measurements were performed in the SDSU and repeated on the X-ray equipment of General Atomic Technology, Inc. of San Diego. Both results were identical. An example of a lauegram from a single crystal $(HgTe)_{0.1}(InSb)_{0.9}$ is presented in Figure 9. The crystal was cut almost perpendicular to the growth direction. One can see a third order symmetry axis almost normal to the photo plane.

2.5. ELECTRICAL CONDUCTIVITY AND HALL EFFECT

For electrical conductivity measurements we used two methods: (a) the so-called collinear four-probe array probe [25] (sample and probe holder type Rig, Model C has been manufactured by A&M, Ltd., England), and (b) the Van-der-Pauw method [26].

The collinear four-probe method was used in our laboratory only for measurements at room temperature. The second method was used

Figure 9. A Lauegram from the $(HgTe)_{0.10}(InSb)_{0.90}$ single crystal taken with the x-ray beam almost parallel to the growth direction. The nearest to the center is the 3-fold symmetry pattern [111].

for measurements in the range from 77 to 300K. The partial derivative evaluation of accuracy gave a magnitude of error in the limits of 3-6% depending upon the sample bulk and surface electrical conductivity and, consequently, the magnitudes of current and voltage drop.

The sign of the dominant charge carriers was determined from the Hall experiments as well as by use of the thermoelectric probe method with a temperature difference between the probes of about 50°C. All grown single crystals and epilayers have had n-type conductivity.

The Hall effect and magnetoresistance measurements were undertaken on the Varian Associate V6060 magnet system (see [6]). The measured magnitude of magnetic induction B_Z was equal to 15 kG. The magnetic induction gradient measurements have shown that the magnitudes of $\Delta B_Z/\Delta X$ and $\Delta B_Z/\Delta Y$ in the limits of the specimen size were smaller than the sensitivity limit of the magnetometer used.

To double check our results of electrical and galvano-magnetic measurement, we asked Dr. Clawson of the Naval Ocean Systems Center (San Diego) to measure conductivity and Hall effect on our specimens. The results of his measurements are in satisfactory accordance with ours (the difference is not greater than 30%). This difference may be explained by distinctions in the contact geometry, existence of adsorption layers on the specimen surfaces in two experimental cycles, local temperature gradients, etc.

2.6. MEASUREMENTS OF OPTICAL AND ELECTROOPTICAL PARAMETERS

This cycle of experiments included investigation of infrared transmission and reflection, and photoconductivity measurements.

The IR transmission and reflection data were used for determination of the cut-off wavelength. The absorption coefficient, k, was calculated from the data on relative transmittance, T, reflectance, R, and the sample thickness, d, using the expression [6]:

$$k = \ln[(1-R)/T]/d \ , \qquad (2.6.1)$$

and the energy gap, ε_g, was estimated on the basis of equation [27, 28]

$$h\nu = \varepsilon_g + C(kh\nu)^2 \ , \qquad (2.6.2)$$

where $h\nu$ is the photon energy and C is a constant, from the extrapolation of the linear part of the curve $h\nu = f[(kh\nu)^2]$ to the interception with the $h\nu$-axis. The magnitude of $h\nu$ in the interception point is equal to ε_g.

In our experiments, T and R were measured at 77K and 300K on the Perkin-Elmer 621 IR Spectrophotometer in the wavelength range from 2.5 to 50 μm. The general view of the dewar used for the low temperature optical measurements is presented in Figure 10.

For the measurements of photoconductivity we chose a CO_2 laser as a source of incident radiation. This choice gave us the opportunity to observe the photoconduction dynamics at the different ratios of $\varepsilon_g/h\nu$. If ε_g is greater than $h\nu$, the radiation generated

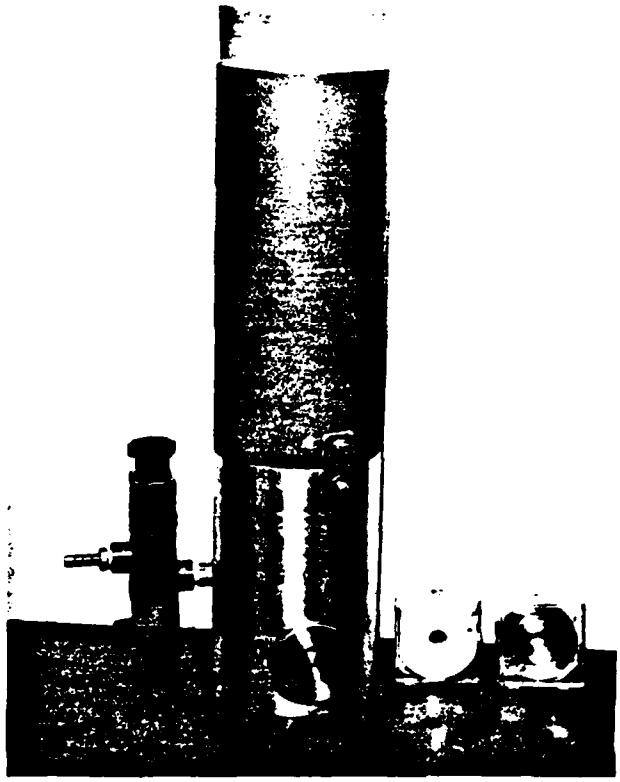

Figure 10. The dewar for low temperature optical measurements.

particles will be produced by the impurity atoms. If $h\nu > \varepsilon_g$, we may assume $\Delta n = \Delta p$. The $(HgTe)_x(InSb)_{1-x}$ crystals investigated had the cut-off wavelength from 7 μm (x = 0) to 14.6 μm (x = 0.2). The CO_2 laser radiation had λ = 10.6 μm which gave us the opportunity to compare photoconductivity in both the cases.

The samples for the measurements (Figure 11) were made in such a way that the direction of the incident beam was perpendicular to the electric current density vector. The omic contacts were made from indium. The symmetry of the dark conductivity was checked with an oscillograph at the frequency 60 Hz.

A sample was connected to the sample holder and dipped in dewar with liquid nitrogen. The sample holder (Figure 12) was designed in such a way that a vertical beam of the IR radiation was first reflected from the right side of the holder under 90° (there was a platinum mirror on that side), and only after it the beam penetrated to the sample. The general view of the photoconductivity measurement device is presented in Figures 13 and 14.

It is known that the thickness of the semiconductor layer that absorbs a definite part of the incident radiation depends upon its absorption coefficient, k. From Lambert-Bouguer's law

$$I = I_0 \exp(-kx), \tag{2.6.1}$$

thickness of a layer that absorbs, say, 99% of the incident radiation is

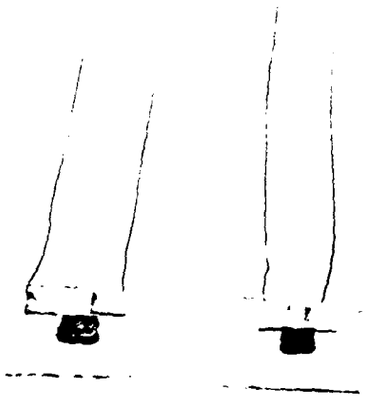

Figure 11. Two specimens for the photoconductivity measurements.

$$x_{0.99} = 4.65/k \qquad (2.6.2)$$

In the case of, for example, InSb, at $\lambda \approx 6$ μm, $k \approx 10^3$ cm^{-1} and $x_{0.99} = 10$ μm. The real thicknesses of photodetectors, l, are usually greater for technological reasons and as a result of it the registered photoconductivity, $\Delta\sigma/\sigma$, or photoresistivity, $\Delta\delta/\delta$, magnitudes are damped; this decreases the accuracy of measurements. Our calculations (see [29] and Appendix) showed that with our geometry of the charge particles and photon motion directions in the sample the signal will be attenuated by magnitude:

$$a = \left(\frac{1}{x_{0.99}}\right)^2 - \frac{1}{x_{0.99}}\left(\frac{1}{x_{0.99}} - 1\right)\frac{\Delta n}{n_o + \Delta n} \qquad (2.6.3)$$

If we consider the number of injected carriers, Δn, independent from l, what is true for $l \tilde{>} x_{0.99}$, the Eqn. (2.6.3) shows that the coefficient of attenuation, a, is proportional to the square of $(1/x_{0.99})$ at $l >> x_{0.99}$.

2.7. THERMAL CONDUCTIVITY

The question regarding the thermal conductivity of the $(HgTe)_x(InSb)_{1-x}$ came up at the time when we started to design our Bridgman-Stockbarger system. The ratio, $k = \kappa_{cr}/\kappa_a$, of crucible to alloy thermal conductivity determines the geometry and kinetics of crystal growth [30-32].

While κ of the binary III-V and II-VI diamond-like compounds was investigated quite thoroughly (see, for example, [33-36], and

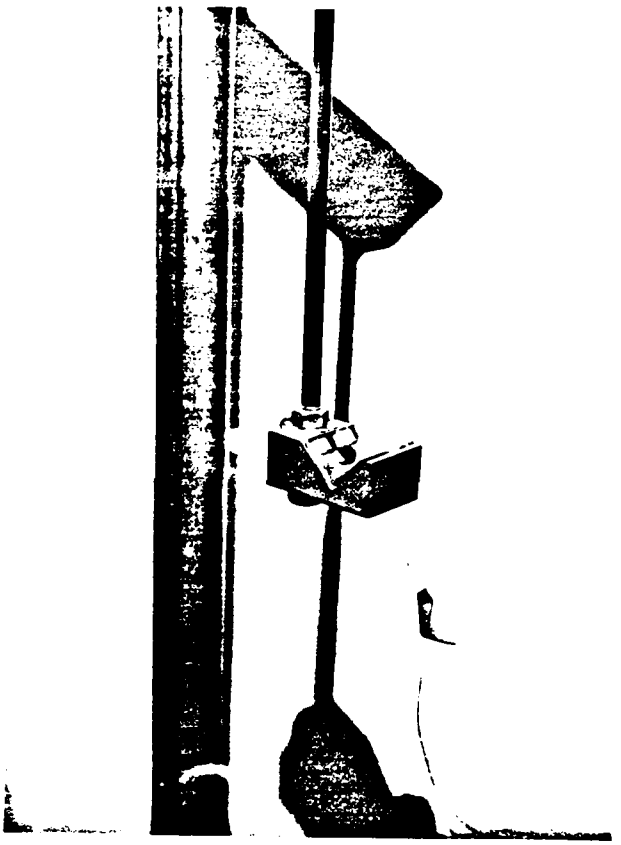

Figure 12. The specimen holder.

Table 1), the problem of their solid solutions does not attract a corresponding attention.

Leibfried and Schloeman [37] derived an expression for lattice thermal conductivity κ_l at $T > \theta_D$ in the form

$$\kappa_l = [\frac{24}{10} \times 4^{1/3} \times (\frac{k_\beta}{h})^3 \times \frac{1}{N_A}] \frac{\overline{M} \cdot \delta \cdot \theta_D^3}{\gamma^2 T} \qquad (2.7.1)$$

where k_β, h, and N_A are the Boltzmann and Plank constants and Avogadro number, M is the average atomic mass, δ^3 is an average lattice volume per atom, θ_D is the Debye temperature, γ is the Grüneisen anharmonicity parameter. At $[\kappa_l]$ = W/cmk, [T] = [θ] = K, [δ] = cm, and [M] = gram

$$\kappa_l = 5.72 \frac{M\delta\theta_D^3}{\gamma^2 T} \qquad (2.7.2)$$

Keyes [38] has shown that κ_l may be expressed as a function of melting point, T_m and density, ρ, in the form

$$\kappa_l = \frac{B\rho^{2/3} T_m^{3/2}}{\overline{M}^{7/6} \cdot T} \qquad (2.7.3)$$

where $B \approx 1/30$ is a constant.

Neither the (2.7.2) nor (2.7.3) expressions are suitable for calculations of κ of a solid solution, because, in general, the latter presents a system of atoms, where different particles in cation and anion sublattices are distributed statistically. Abeles [39]

TABLE 1. SUMMARY OF DATA ON SOME II-VI AND III-V DIAMOND-LIKE COMPOUNDS

Material	InSb	HgTe	CdTe	InAs
Average Atomic Mass, g/mole	118.4	164.10	120.0	94.8
Bond Energy, eV	5.5		4.3	6.4
Debye Temperature, K	202	114.3	200	249
Thermal Expansion, 10^{-6} K^{-1}	4.67			4.68
Density, g/cm^3	5.78	8.07	5.87	5.68
Melting point, K	809	943	1314	1215
Gruneisen parameter	1.04			1.07 (1.15)
Thermal Conductivity, W/cmK	0.165	0.021	0.060	0.265
Linear size per atom, $V_a^{1/3}$ Å	3.239	3,215	3.240	
Microhardness, kgp/mm^2	220	20	60	330
Ionicity, % [44]	2		15	

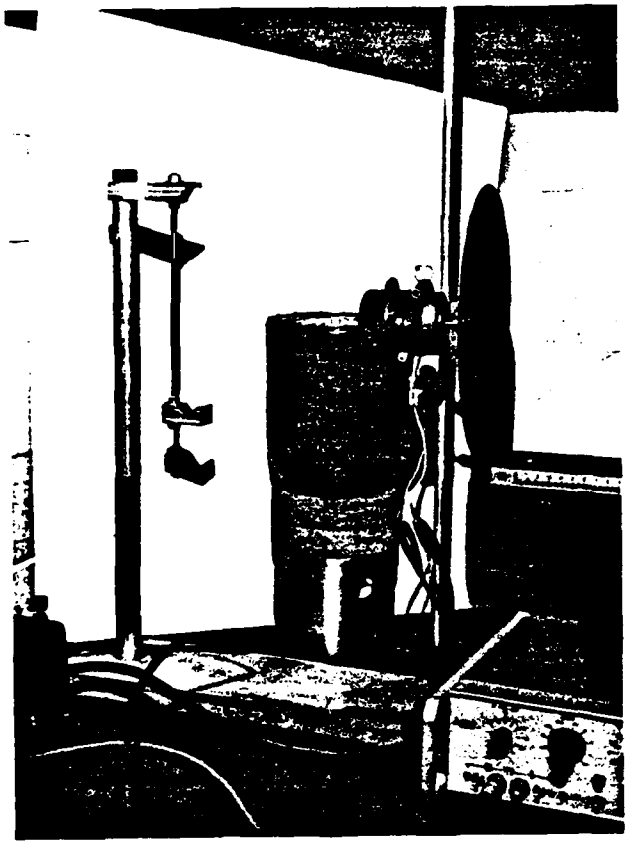

Figure 13. A part of the photoconductivity device. From the left: the sample holder, the dewar, the chopper, and the amplifier.

offered a model of solid solution as a random mixture of atoms and calculated, on this basis, κ of solid solutions in the Ge-Si and GaAs-InAs systems at high temperatures in satisfactory agreement with the experimental results. In his model, κ is expressed in terms of the lattice parameters and mean atomic masses of the alloy and its constituents. In his work, Abeles used a simple phenomenological model of thermal conductivity, developed by Klemens [40] and Callaway and Baeyer [41]. In the limit of strong point-defect scattering, which is realistic for a disordered solid solution, Abeles gives expression

$$\kappa = [9.67 \times 10^{5} (1 + 5\alpha/9)^{1/2} \gamma \cdot \beta^{-2} \Gamma^{1/2} \bar{M}^{1/2} \delta^{3} T^{1/2} +$$

$$+ 7.08 \times 10^{-2} (1 + 5\alpha/9) \gamma^{2} \beta^{-3} \bar{M}^{1/2} \delta^{7/2} T]^{-1} \qquad (2.7.4)$$

where α is a parameter that depends on the phonon relaxation time, γ is the Grüneisen anharmonicity parameter, β is a parameter that depends on Debye temperature, average atomic mass, M and a lattice parameter, $\delta = a/2$, (β is nearly constant within a given covalent crystal system), Γ is a parameter that depends on the difference in atomic masses of the constituents of the alloy, $\Delta M = M_A - M_B$, the alloy composition, x, and difference of lattice parameters, $\Delta\delta$:

$$\Gamma_i = x_i \{(\Delta M_i/M)^2 + \varepsilon[(\delta - \delta_i')/\delta]^2\} \qquad (2.7.5)$$

$$\Gamma = \sum_i \Gamma_i, \qquad (2.7.5)$$

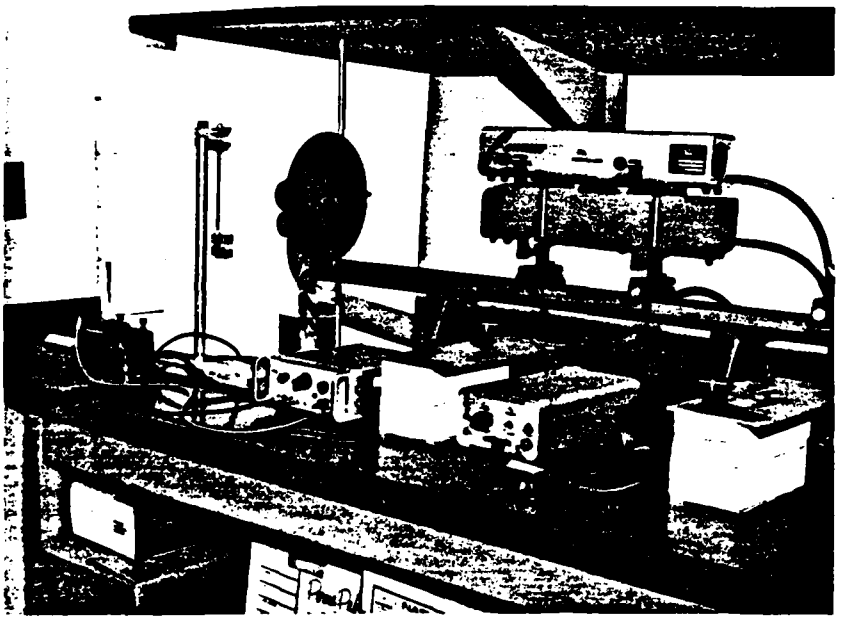

Figure 14. The photoconductivity measurement device. Shown from left to right: galvanometer (or recorder), sample holder, chopper, amplifier, CO_2 laser on the optical bench, and the laser power supplier under the bench.

and ϵ is a phenomenological, adjustable parameter ($\epsilon \approx 40$). In the case of a mixture of two kinds of atoms, A and B, Eqns. (2.7.5) and (2.7.6) give:

$$\Gamma = x(1-x)[(\Delta M/M)^2 + \epsilon(\Delta\delta/\delta)^2] \qquad (2.7.7)$$

Berger et al. [42] used Abeles' expression (2.7.4) and found that it was in satisfactory agreement with the results of their measurements of κ of the InSb - InAs alloys.

For our measurements of thermal conductivity we used a transient, relative method developed by the Ioffes [43]. The measurements took place at the temperature close to 285 K. The general view of the measurement device is presented in Figure 15. The accuracy of the experiment was close to 15%.

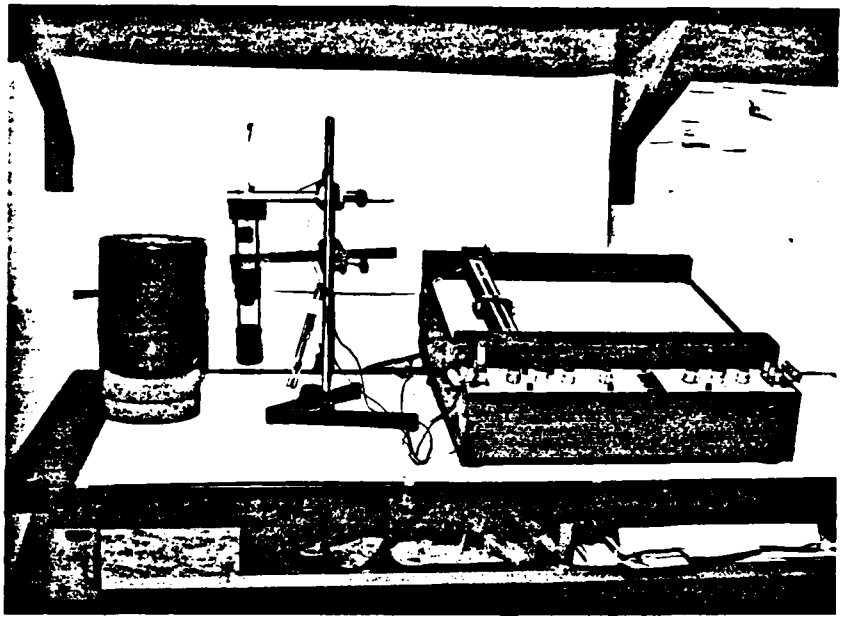

Figure 15. Thermal conductivity measurement device. The sample holder with the heat source and sink is shown between the dewar and recorder.

3. RESULTS

3.1. SINGLE CRYSTAL GROWTH

In the majority of runs, we have grown single crystals with the length of the first from the tip crystal not less than 75% of total length of the load. Our experiments have shown that the shape of the ampule tip did not play any important role in the process of growth, at least with the flat angle at the tip smaller than 90°. The explanation for it we see in the substantial uniformity of temperature in the limits of each part of the Bridgman furnace, achieved by using thick metallic pipes in them. Szofran and Lehoczky [45] in their experiments with HgCdTe had the same results. As was discussed in [46], the curvature of isotherms in the liquid and solid parts of the load are opposite in the case of a semiconductor, because the latter has a substantially greater thermal conductivity in the solid state compared with that of the liquid, and the ampule walls transfer a significant amount of heat. The isotherms in the upper part are concave upward and that in the solid part have an opposite orientation. Their curvature decreases to the crystallization front, and somewhere near it we have an isothermal plane. It is interesting to mention that in accordance with [45] the thick-wall quartz ampules provide some advantages for the process of growth of high quality semiconductor crystals.

The maximal speed of growth which permitted us to grow satisfactory quality crystals was v_{cr} = 1.1 μm/s. We found that temperature gradient near the interface could be as low as 22°/cm at the

TABLE 2. SINGLE CRYSTAL GROWTH

Run No.	Composition, % (mole)		Temperature, K			Single Crystal Length, mm	Lowering Rate cm/hr	Comments
	HgTe	InSb	Hot Zone	Cold Zone	Anneal-ing			
1	2	3	4	5	6	7	8	9
1	5	95	910	783	783	--	0.2	Polyphase structure, black powder inclusions
2	5	95	900	773	700	20	0.3	Single crystal in the tip of ampoule
3	5	95	810	770	700	10 (tip)	0.4	Single crystal, surface looks oxidized, the ampoule has a crack
4	5	95	810	770	770	15	0.4	Shiny surface, large crystal, amorphous deposition on top
5	5	95	810	770	490	40	0.4	Single crystal, no depositions, no cracks
6	10	90	850	753	753	--	0.3	Polycrystal, powder inclusions, mercury drops
7	10	90	795	668	668	--	0.3	Polycrystal

TABLE 2. Continued

1	2	3	4	5	6	7	8	9
8	10	90	803	763	763	10	0.4	Single crystal in the conic part
9	10	90	803	763	673	30	0.4	Single crystals, no cracks
10	12	88	802	730	730	--	0.4	Hg droplet on the surface, polycrystal
11	12	88	786	710	710	43	0.4	Single crystal; little spots of mercury
12	12	88	802	730	730	--	0.4	The ampule was broken
13	12	88	772	706	706	20	0.4	No free mercury, shiny surface
14	12	88	802	728	728	--	0.4	Polycrystal
15	12	88	803	710	573	40	0.4	Single crystal
16	12	88	786	710	670	--	0.4	Polycrystal
17	12	88	800	723	690	73	0.4	No free mercury, shiny surface

TABLE 2. Continued

1	2	3	4	5	6	7	8	9
18	12	88	800	725	670	--	0.4	Ampule was broken
19	15	85	800	730	670	--	0.4	Polycrystal
20	15	85	788	710	670	15	0.4	Single crystal, smooth and shiny

speed $v < v_{cr}$. From our point of view, an important factor that determines the success of the growth process is a condition that

$$\frac{\delta^2 T}{\delta Z^2} = 0 \qquad (3.1.1)$$

on both sides of the interface and especially above it. We believe that the condition (3.1.1) is connected to the temperature dependence of thermal conductivity of the melt.

In general, a greater temperature gradient in the melt near the surface of a growing crystal is followed by an increase in the defect density, primarily that of dislocations. During the reported year, we did not have a proper method for defect evaluation, therefore we charcterized the crystal defectiveness from electrical transport properties. Our experiments showed that the best uniformity of the $HgTe_{.12}InSb_{.88}$ parameters was reached at the temperature gradient equal to 22°/cm and $d^2T/dZ^2 = 0$ from 5 mm below the interface to 15 mm above it, in the liquid.

The uniformity of the crystals was controlled metallographically and by the microhardness measurements. It was shown that the radial uniformity was better in the crystals that had greater total length at the same crystal diameter. Also, it was established that the crystal radial uniformity is better at a smaller ratio of the crystal diameter to that of the metallic inserts in the Bridgman furnace. We believe that for a given load mass it is advantageous to grow a long thin crystal in a furnace of a relatively large

diameter. It is clear also that the interface concavity may be reduced if the furnace has a lower longitudinal temperature gradient in the interface gone. A shallow temperature gradient and a relatively slow motion of the ampule permit to the crystal to be annealed to the state at which volatile components first and foremost will have low mobility.

3.2. EPITAXIAL GROWTH

The epitaxial layers of HgTe on the InSb substrates were prepared by the following reactions

$$HgTe_{(source)} \rightleftarrows Hg_{(gas)} + 1/2\ Te_{2(gas)}$$

$$Hg_{(gas)} + 1/2\ Te_{2(gas)} \rightleftarrows HgTe_{(c.,\ substrate)} \cdot$$

The substrate had orientation (111). The reactor for the hot-wall epitaxy had two temperature zones which were independently controlled to within ± 1K. As the source material we used HgTe shot (Poly Research Corporation). After wet polishing to a surface finish of about 0.4 μ with alumina powder, the substrates were etched with a bromine-methanol mixture and thoroughly rinsed with DW.

The heating of the substrate, source and wall started with the shutter (Figure 3) in the closed position. When the temperature

reached the chosen magnitudes, the shutter was opened to start the growth process.

Dependence of the growth rate on the source temperature is close to the exponential one (see Figure 16). Apparently the molecule kinetic energy in the process of deposition plays a secondary role in comparison with the partial pressure of the gas phase components and/or their concentration near the substrate. Quality of the deposited layers depended upon the substrate temperature as well as on the source temperature. In Figure 17 one can see the substrate-source temperature field in the limits of which our experiments were finished with the epitaxial layers. Outside of the field, the experiments were ended with the growth of a polycrystalline or amorfous film or without any deposition.

In accordance with Zemel [47], for the source and substrate of the same material, the rate of deposition, R_d, is

$$R_d = (P_{so}T_{so}^{-1/2} - P_{su}T_{su}^{-1/2})\ \alpha/(2\pi mk)^{1/2} \qquad (3.2.1)$$

where P is pressure, α is a coefficient that depends on the condition of the surface, m is the mass of a molecule, k is the Boltzmann constant, and the subscripts so and su relate to source and substrate respectively. The Eqn. (3.2.1) is written on the basis of some assumptions that make its effective use quite difficult especially for alloys. The only condition we may consider always valid is that vapor pressure in the space near a substrate must be greater than

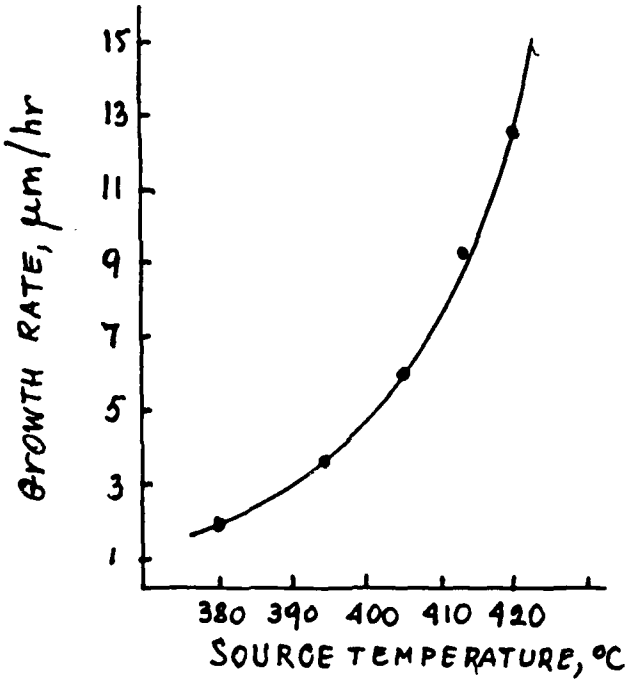

Figure 16. Growth rate as a function of the source temperature.

the equilibrium pressure of the material evaporating from the substrate [10] and greater of a critical magnitude:

$$P/P_e > (P/P_e)_{cr} . \qquad (3.2.2)$$

The results of our experiments with the HWE show that the deposited films are epitaxial if they were grown at the magnitudes of T_{su} and T_{so} that belong to the points of the plot T_{su} (T_{so}) in Figure 17 laying inside of the closed curve. Roughly speaking, with our experimental geometry, epitaxial growth will take place if the magnitudes of T_{su} and T_{so} lay inside of a triangle with coordinates of vertices: (1) T_{su} = 210, T_{so} = 340; (2) T_{su} = 380; T_{so} = 410; (3) T_{su} = 340 and T_{so} = 460°C.

Our experiments with evaporation-diffusion in a close volume at isothermal conditions have an important difference from experiments on HgCdTe which consists in (a) a very big difference in the vapor pressure of the source components, Hg and Te, in comparison with the substrate components, In and Sb (Table 3), and (b) absence of a common component (say, anion) that may migrate in both directions between the source and substrate. In our experiments, the temperature in the reaction volume was 350 ± 50°C. At these temperatures, a predominant component of the gas phase was mercury. When a fast Hg atom (pressure about 250 mm) reaches the substrate surface, it interacts with the anion sublattice first, because of the higher partial pressure of the Sb atoms. As a result of this interaction, the surface of InSb will be covered with a layer of the Hg atoms in

TABLE 3. VAPOUR PRESSURE OF SOME ELEMENTS

Substance	Pressure, Torr						Melting Point, °C
	1	10	40	100	400	760	
	at temperature, °C						
Mg	126	184	229	262	323	357	-38.9
Sb	886	1033	1141	1223	1364	1440	630.5
Te	520	633	753	838	997	1087	452
In	1264	1366	1568	1740	1960	2080	156.6
Ga	1349	1541	1680	1784	1974	2071	30
Cd	394	484	553	611	711	765	320.9
Sn	1492	1703	1855	1968	2169	2270	231.9

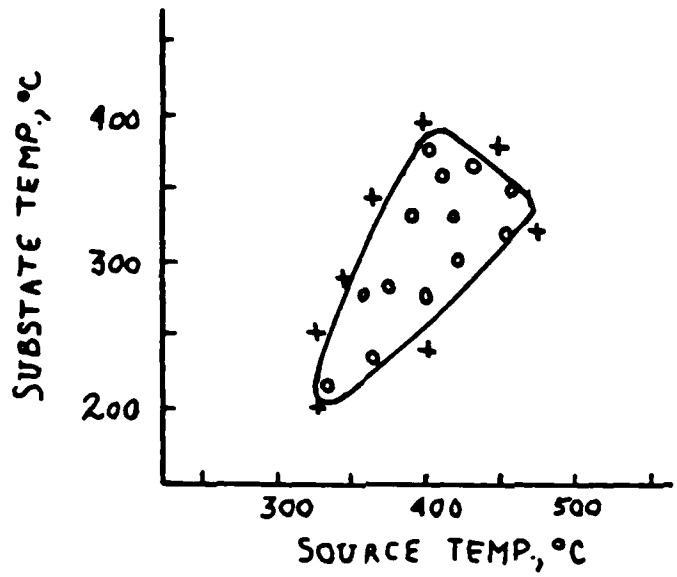

Figure 17. Graphical representation of the HWE experiments. The circles represent the experimental conditions for the epitaxial growth; the crosses represent T_{su} and T_{so} for polycrystal deposition or lack of deposition. The area surrounded by the closed curve is a T_{su}-T_{so} field for the epitaxial growth of $(HgTe)_x(InSb)_{1-x}$.

both "cationic" and "anionic" positions. Cohesive force between atoms of Hg and In is substantially smaller than that of Hg and Sb (for example, the highest melting point in the phase diagram Hg-In is 108°C in comparison with 450°C for the only [hypotetic] compound Hg_3Sb_2 in the Hg-Sb system). Consequently, Hg atoms will sublimate from "anionic" position, giving an opportunity for their occupation by the Te atoms from the vapor phase. This process will be finished with the creation of a layer of HgTe on the surface of InSb. Atoms of Hg and In, as well as Te and Sb, will migrate in the mutually opposite directions toward the negative concentration gradient, that will be followed by the creation of the possibility of the new HgTe layer deposition. One can see from this mechanism that rate of deposition of the absorbed layer will be controlled by the partial pressure of Te in the reaction volume and its amount in excess to the stoichiometric composition [51]. The authors of [14] came to the same conclusion which gave us reason to believe that in both HgCdTe and HgTeInSb layers the limiting role belongs to the least volatile component of the source material.

The probability of mutual diffusion is very high for all four kinds of atoms if we consider their size as one of the "covalent" atoms. Palatnik et al. [50] offered the following magnitudes of the "true covalent tetrahedral radii": r(Hg) = 1.545; r(In) = 1.485; r(Sb) = 1.350; and r(te) = 1.280A. These data agree with the results of the x-ray measurements better than any other known, including, of course, the Hg^{+2}, In^{+3}, Te^{-2}, and Sb^{-3} radii [8].

TABLE 4. GROWTH PARAMETERS OF HgTe ONTO InSb SUBSTRATES

Sample No.	Temperature, K	Av. Growth Rate, A/hr	Time, h	Thickness, μm	Film Weight, mg
1	573	830	196	16	10.2
2	623	1670	148	25	16.0
3	723	2900	76	22	14.1

In our experiments, the deposition time was varied from 24 to 196h. The average thickness of the layers, as measured by weighing the samples before and after deposition, was proportional to the square root of the deposition time. For the thickness calculations, we assumed that the deposited layer had the shape of a straight cylinder and the mass density of the grown material was equal to 8.17 g/cm^3. The results of some of our experiments are presented in Table 5.

On the first stage of growth, the triangle centers of deposition appeared on the surface of the substrate, followed by their mergence and formation of a monolytic layer. If a part of the initial triangles did not have the same orientation on the surface of substrate, the growing layer had little spots on it or all its surface was darker in comparison with the successful runs.

The best results were obtained at 350°C and the deposition time close to 6 days. Under these conditions, the films were dense, mirror-like, and possessed the best electrical properties. All grown films were of *n*-type conductivity. It draws us to the conclusion that the intensive interdiffusion took place during the growth process, because otherwise the as-grown layers would have p-type conductivity without an additional amount of metallic Hg in the growth volume [52]. A detailed investigation of the diffusion process is one of the subjects of our future work.

3.3. MICROSTRUCTURE AND MICROHARDNESS

The surface morphology of crystals and films was examined by optical microscopy. It was established that creation of the epitaxial deposition centers depends upon the surface etching prior to the deposition.

We used the $1HF:1HNO_3$ etchant [53, 54] to avoid the polishing effect. In both HWE and EDRI processes, the first centers of the epitaxial deposition appeared faster and with fewer irregular oriented ones among them if the substrate was etched for 5 seconds once (EDRI) or twice (HWE). A typical view of the substrate surface after the etching is shown in Figure 18 (100^X). One can see that the average size of the etch pits is quite uniform; it is equal to about 15 μm. It gives us the average depth in the center of a pit of about 4 μm [55].

The surface uniformity of the grown single crystals was evaluated by the microhardness, H, measurements (Table 7). Our experiments with both HWE and EDRI grown epitaxial layers gave us a magnitude of H close to 50 ± 15 kgp/mm , which is slightly higher than H of pure HgTe. It means that the interdiffusion of HgTe and InSb in the epilayers and substrates has not been completed yet. This task is part of our plans for the next year of work with this project.

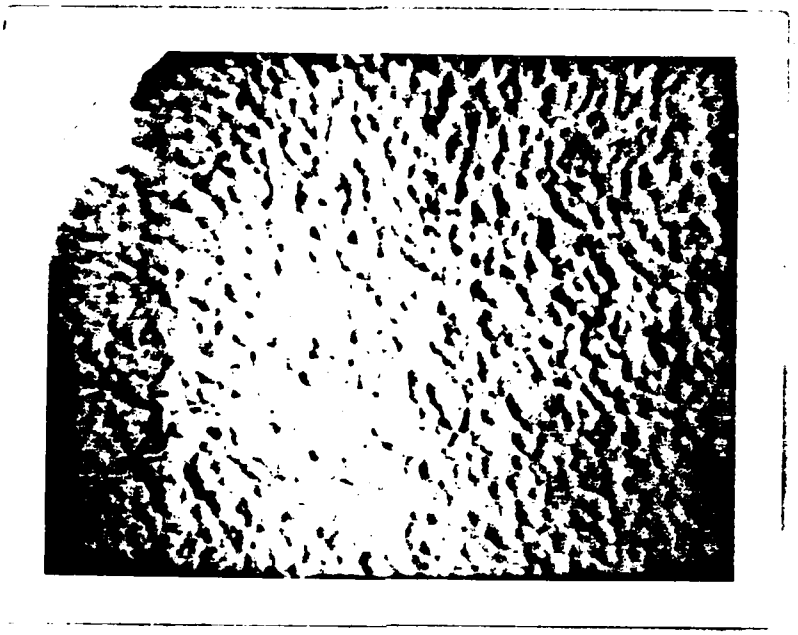

Figure 18. A substrate surface after the etching (100^{X}).

3.4. X-RAY ANALYSIS

The X-ray analysis was used for investigation of the single crystal size, as a supplement to the microstructure and microhardness investigation, and the single crystal growth direction. We made the Laue photos from the slices of a single crystal that were cut with the ampule in the direction of its growth. The first slice, which had a change in the position of the diffraction maxima or had an additional set of maxima, was considered as a border of the initial single crystal.

Investigation of segregation was done by the Debye-Scherrer X-ray analysis on the powder that was made from the crumbs taken from different points of a grown single crystal along its axis and perpendicular to it. These results were then compared with the X-ray Debye-Scherrer data which were received from the polycrystals of a definite composition. Discrepancy between the results on the polycrystals and single crystals of the same composition (or expected composition) did not exceed 0.3%. The accuracy in evaluation of the lattice parameter, a, increases with the increase of Bragg's angle, θ, in accordance with the ratio

$$\Delta a/a = \pm \Delta\theta/\tan\theta \qquad (3.4.1)$$

One of the common ways to get the precision magnitude of a is the extrapolation of the curve $a = a\ (\cos^2\theta)$ to the magnitude $\cos^2\theta = 0$.

The results of our investigation of the grown crystals are presented in Tables 5 and 6. We believe that in the case of the

TABLE 5. LATTICE PARAMETERS FROM X-RAY DIFFRACTION

Substance	θ, degree	Peak Intensity, %	d_{hkl}, Å	hkl	a, Å	a, Å Extrapolation to $\cos^2\theta=0$	a, Å Extrapolation to $\sin\theta=1$
InSb single crystal	23.960	99.47	3.7108	111	6.4273		
	39.503	95.87	2.2792	220	6.4466	6.482	6.485
	46.627	100	1.9463	311	6.4551		
	56.967	21.79	1.6151	400	6.4604		
$(HgTe)_{0.05}(InSb)_{0.95}$	24.026	73.91	3.7007	111	6.4098		
	39.574	100	2.2753	220	6.4355	6.475	6.462
Single crystal	46.786	49.06	1.9400	311	6.4343		
	--*						
$(HgTe)_{0.10}(InSb)_{0.9}$	24.076	59.46	3.6932	111	6.3968		
	39.726	100	2.2670	220	6.4120	6.488	6.457
Single crystal	46.888	23.93	1.9360	311	6.4210		
	57.296	13.53	1.6066	400	6.4264		
$(HgTe)_{0.12}(InSb)_{0.88}$	24.017	100	3.7021	111	6.4122		
	39.612	54.80	2.2732	220	6.4296	6.456	6.455
	46.800	41.70	1.9395	311	6.4326		
	57.190	8.17	1.6094	400	6.4376		

*The computer did not print out the fourth peak.

HgTe-InSb system, the difference in composition between solid and liquid phase is not as great as in HgCdTe because the phase diagram of the former system [6] shows a much smaller distance between the solidus and liquidus curves than that of the latter.

Our experiments with single crystals were concentrated mainly upon three compositions: $x = 0.05$, $x = 0.10$, and $x = 0.12$. The reason for this is in the fact that these alloys cover the most important wavelength range for far-infrared detection: from 7 to 12.0 μm. In the alloys with greater cut-off wavelength, the tunneling effects play an important role; however, this problem remains outside the limits of this project.

The Laue X-ray analyses show that all primary single crystals grow in the direction [111] with a maximum decline from it less than 2.5°. The successfully grown epitaxial layers repeated the InSb substrate orientation, (111), with a deviation smaller than the experimental error.

From Table 7 one can see that the radial uniformity of microhardness, H, is quite high: deviations from an average magnitude are in the limits of the experimental accuracy. Comparison of the results with the measurements of H on the polycrystals [6, p. 26] shows, in accordance with the theoretical predictions [56], that the magnitudes of H of single crystals are greater in comparison with the polycrystals of the same composition. One more interesting feature of the results consists of a shift of the maximum H to the greater magnitudes of x: from about $x = 0.09$ for polycrystals to

TABLE 6. PARAMETERS OF THE GROWN CRYSTALS

Initial Composition, mole, %		Size of the Single Crystal Part, mm		Lattice Parameter, Å	Microhardness, H, kgp/mm^2	Radial dispersion of H %
HgTe	InSb	Diam.	Length			
5	95	10	40	6.462	250	2
10	90	10	30	6.457	261	2
12	88	10	40	6.455	272	2

about x = 0.12 for single crystals. The last effect may be considered as an indirect evidence for the conception that the HgTe-InSb section of the Hg-In-Te-Sb quarternary system is not a quasibinary one. This conception, however, needs some additional investigations, which are outside the limits of this project. The greater magnitudes of H of single crystals are in accordance with the results of Ablova and Feoktistova [57], who showed that InSb has the greatest H on the plane (111).

3.5. ELECTRICAL AND GALVANOMAGNETIC PROPERTIES

In our measurements we used as a standard the electrical and galvanomagnetic properties of the InSb single crystals of Poly Research Corporation which had an electrical conductivity in the limits $18.2 \leq \sigma \leq 58.8$ 1/Ohm cm, concentration $2.1 \times 10^{14} \leq N_D - N_A \leq 10.0 \times 10^{14}$ $1/cm^3$, and mobility, μ, from 3.6×10^5 to 5.5×10^5 $cm^2/V \cdot sec$ at room temperature.

Our measurements were conducted at 77 K and 300 K. In a majority of the Bridgman-grown crystals, the highest magnitudes of μ were related to the slices that were cut out at the end of the conical part of the ampule. As mentioned before, all grown crystals had the n-type conductivity. The averaged results of the measurements are presented in Table 8. In all cases Hall measurements demonstrated the n-type conductivity. From the change of mobility with temperature it is possible to conclude that scattering is controlled mainly by the ionized impurities. The donor ionization energy shown in

TABLE 7. MICROHARDNESS OF THE $(HgTe)_x(InSb)_{1-x}$ SINGLE CRYSTALS

Composition X	Microhardness, kgp/mm^2, vs. Distance from the Center, mm							Average kgp/mm	Deviation % (max.)	H (Poly-Crystal), kgp/mm^2, Average
	-3	-2	-1	0	1	2	3			
0.00	230	229	234	236	236	237	226	233	3	201
0.05	248	250	250	248	254	252	250	250	2	238
0.10	266	265	258	258	262	253	267	261	2	244
0.12	267	275	271	278	272	269	272	272	2	215
0.15	258	258	263	265	263	267	261	262	2	201

Table 8 was determined from the Hall coefficient data. Apparently the range from 77 K to 3000 K is a transition region between extrinsic and intrinsic conductivity (6.6 meV $\leq k_B T \leq$ 2.58 meV).

The electrical properties of the films grown both by the hot-wall epitaxy, HWE, and by the EDRI method were typical for the HgTe films (see, for example [58, 59]).

We assume that the results of our measurements depend not only on the film quality itself but also on (a) its thickness, because the InSb substrate had a relatively high conductivity, and (b) the depth of diffusion of the deposited atoms into substrate. The results of our measurements of the film electrotransport parameters together with the data on substrate measurements prior to the deposition are presented in Table 9. One can see from the data that the electrical properties of the layers are lower in comparison with the bulk crystals. We believe that the films have substantial transitional layers with high concentration gradients and with high defect contents, mainly, point (vacancies) and one-dimensional (dislocations) defects. The fact that all films had n-type conductivity may be considered as an indirect proof of the strong influence of the substrate on the results of the measurements, because usually as-grown epitaxial HgTe layers exhibit p-type conductivity without an excessive amount of mercury in the gas phase [14, 52] or in the liquid source [60].

TABLE 8. THE AVERAGED RESULTS OF ELECTRICAL AND GALVANO-MAGNETIC MEASUREMENTS

	σ, (Ohm cm)$^{-1}$		R_H, cm^3/C		$N_D - N_A$, cm^{-3}		μ_H, 10^3cm^2/V·sec		0.018 $\ln(n_{300}/n_{77})$,
X	77K	300K	77K	300K	77K	300K	77K	300K	eV
0.00	18.9	48.1	27200	6700	2.3E14	9.3E14	513	323	0.025
0.00	566	1.43x10	368	110	1.7E16	5.7E16	208	157	0.022
0.10	581	906	298	114	2.1E16	5.5E16	173	103	0.017
0.12	797	1160	189	88	3.3E16	7.1E16	151	102	0.014

3.6. OPTICAL TRANSMITTANCE/REFLECTANCE AND PHOTOCONDUCTIVITY

The results of our measurements of optical transmittance and reflectance were used for the calculation of the energy gap in accordance with Eqns. (2.6.1) and (2.6.2). The magnitude of ε_g as a function of HgTe contents is presented in Figure 19. It is interesting to note that, in general, magnitudes of ε_g of single crystals are slightly higher than those of polycrystals of the same composition [6, p. 63]. Analysis of the experimental curves $T = f(\lambda)$ and $R = \phi(\lambda)$ for two kinds of samples showed that at greater electron concentrations, typical for polycrystals, R is changing only slightly whereas T is decreasing substantially. It is followed by the growth of the second member of rhs of Eqn. (2.6.2) and by a corresponding decrease of ε_g. Measurements were made only on the samples prepared from the bulk single crystals. All attempts to make thin samples of the deposited films were unsuccessful. Comparison of different samples shows that annealing of the crystals increases their transmittance and creates a sharp transmission edge.

The photoconductivity measurements on the single crystals and epitaxial layers were undertaken with the samples immersed in the dewar with liquid nitrogen. The average intensity was controlled by the thickness of the N_2 layer upon the sample and the diameter and location of the chopper opening. Dependence of photoconductivity $\Delta\sigma/\sigma$ on the the illumination intensity can be written for an n-type sample in the form [61]

TABLE 9. ELECTRICAL PROPERTIES OF THE EPILAYERS AND SUBSTRATES AT 300K

Sample No.	Thickness, μm	μ, $cm^2/V \cdot sec$		N_D-N_N, cm^{-3}		Comments
		Layer	Substrate	Layer	Substrate	
8/1	16	1.8E3	3.4E5	2.2E18	8.E14	Average of 6 measurements
13/2	25	2.9E3	4.1E5	9.1E17	6.3E14	Of 4 measur.
14/3	22	2.3E3	4.9E5	8.3E17	5.7E14	Of 5 measur.

$$\Delta\sigma/\sigma = \eta I \tau_p (1 + \frac{\mu_n}{\mu_p})/(n_o t) \qquad (3.6.1)$$

where η is the quantum efficiency, I is the Poynting vector magnitude of the incident light, τ_p is the nonequilibrium carrier lifetime, n_o is the equilibrium electron density, and t is the thickness of the sample. Results of our measurements are in satisfactory agreement with Eqn. (3.6.1). From Figure 20 one can see the linear dependence between $\Delta\sigma/\sigma$ and I. Relatively low photoconductivity of the InSb and $(HgTe)_{0.05}(InSb)_{0.95}$ samples may be considreed as evidence that photoresponse for these samples is the result of interaction of the incident photons with the acceptor levels. In the process of our measurements we observed the existence of saturation of the photoconductivity signals in strong electric fields. The curves in Figure 20 represent photoconductivity in the nonsaturated field part.

The photoconductivity relaxation time, τ, for all investigated samples was independent of the incident radiation intensity. The τ remained constant within the limits of the experimental accuracy for the samples with a low sensitivity, and decreased with the electric field increase in the samples of higher sensitivity. A detailed investigation of the photoconductivity parameters is a part of our plans for the next year.

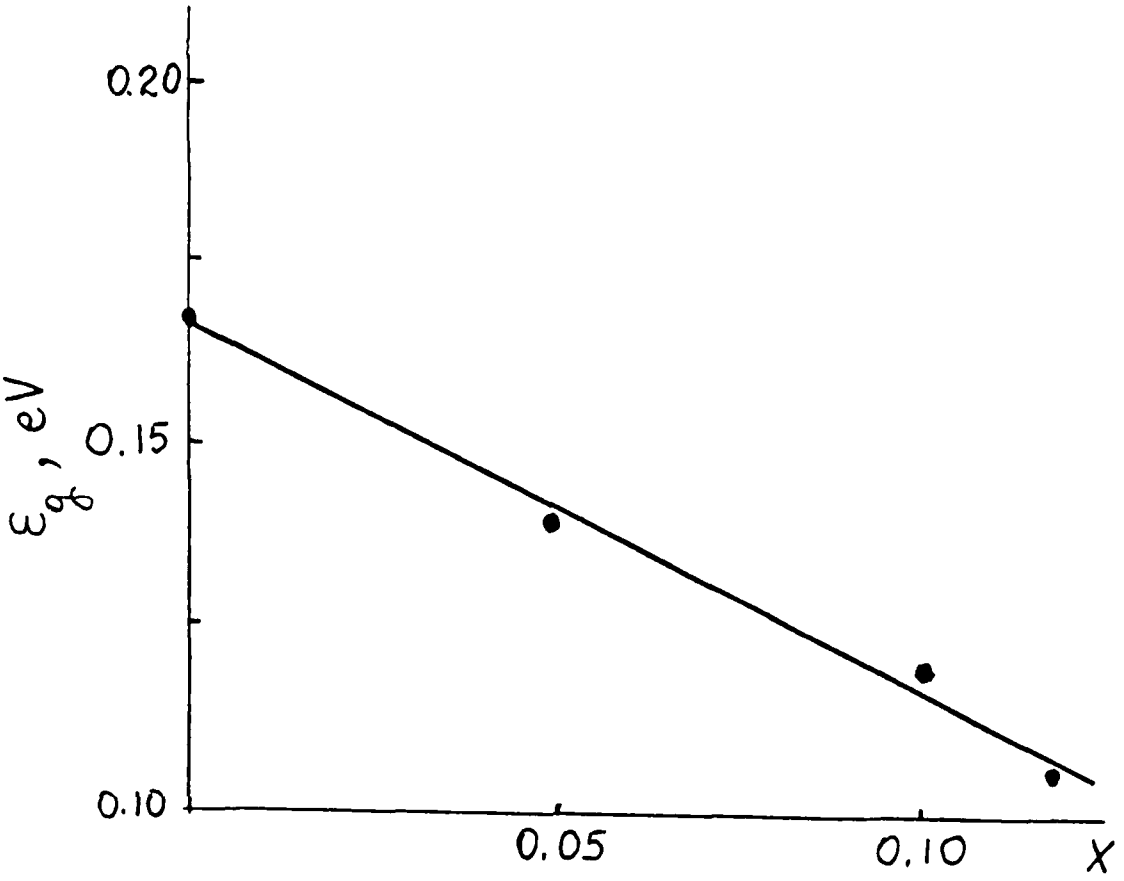

Figure 19. Dependence of the optical energy gap on the alloy composition at 300 K.

3.7 THERMAL CONDUCTIVITY

The results of our measurements of thermal conductivity, κ, on a series of $(HgTe)_x(InSb)_{1-x}$ crystals are presented in Table 10. The difference in κ of the InSb single crystals and polycrystals is about 10%, which is within the expected limits. We calculated κ on the basis of Abeles' model [39], taking data from Table 1 and using formulas (2.7.4, 5, 6). The dashed curve in Figure 21 was computed with $\alpha = 2.5$, $\beta = 1.41 \times 10^{-8}$ K·cm$^{3/2}$, $\gamma = 1.8$, and $\varepsilon = 42$. One can see that the experimental curve has a minimum between $x = 0.10$ and $x = 0.15$ which agrees with the microhardness maximum (Table 7), but the computed curve apparently has a minimum (a thermal resistivity maximum) close to the central ordinate of the phase diagram. It is a direct consequence of the fact that the model used for computing is essentially that of an isotropic elastic continuum and all Γ_i's in (2.7.6) will have a maximum closer to $x_i = 0.5$. In the calculations of the disorder scattering relaxation time, Abeles assumed that multiple scattering could be neglected. Nevertheless, the magnitudes of experimental and calculated κ are in satisfactory agreement within the limits $0 \leq x \leq 15$.

Electronic contribution to the thermal conductivity was evaluated on the basis of the Wiedemann-Franz law

$$\kappa_e = L\sigma T \qquad (3.7.1)$$

and assumption of the dominant acoustic deformation potential

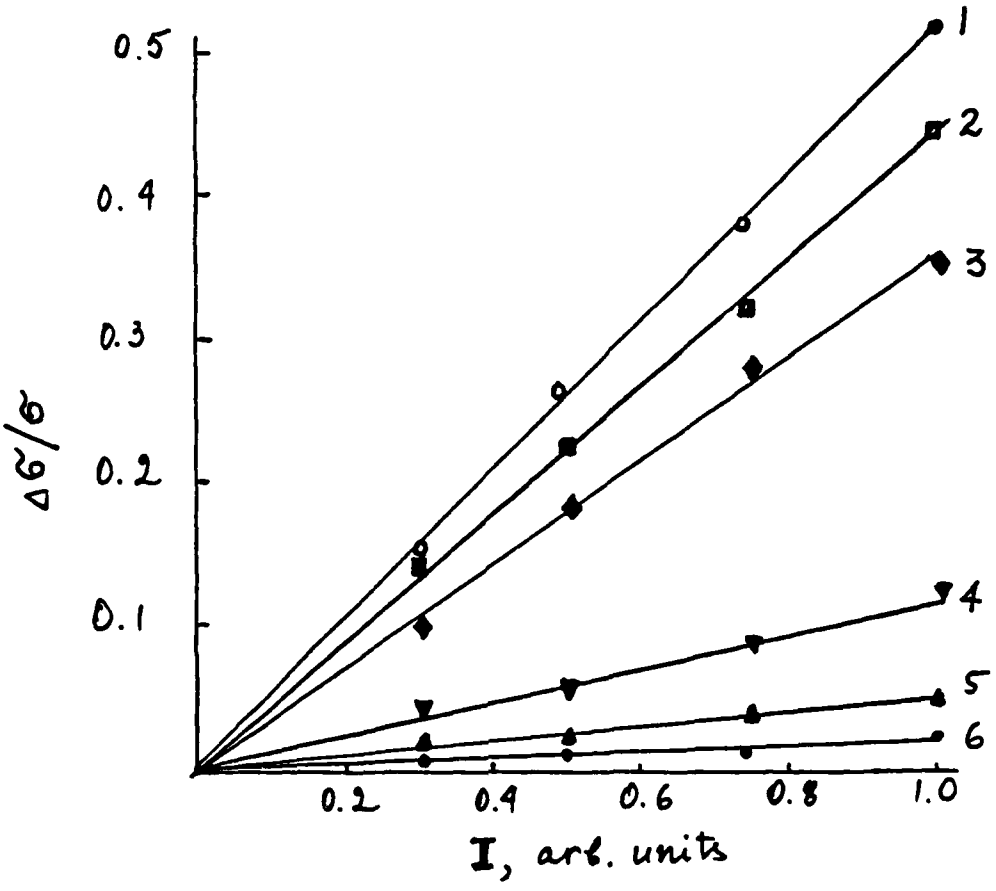

Figure 20. Dependence of photoconductivity on the illumination intensity. The curves 1, 3, 5 and 6 are for the single crystals with x equals to 0.12, 0.10, 0.05, and 0.00 respectively; the curves 2 and 4 are for an EDRI sample and an HWE sample respectively.

TABLE 10. THERMAL CONDUCTIVITY OF $(HgTe)_x(InSb)_{1-x}$ SINGLE CRYSTALS

Sample	Recorded Time, Sec, at the Run No.										κ, mW/cm K Average from 10 runs	Maximum Deviation, mW/cm K	
	1	2	3	4	5	6	7	8	9	10		$-\Delta\kappa$	$+\Delta\kappa$
InSb (single)	2.4	2.4	2.7	2.9	2.9	3.2	2.8	2.7	2.7	2.3	155	8	5
$(HgTe)_{0.05}(InSb)_{0.95}$	6.0	6.6	6.0	6.1	5.7	6.1	6.0	7.1	7.2	6.5	119	3	2
$(HgTe)_{0.10}(InSb)_{0.90}$	10.3	9.2	10.2	11.2	11.3	9.3	9.9	10.4	11.6	9.6	109	2	2
$(HgTe)_{0.12}(InSb)_{0.88}$	12.2	13.7	13.5	13.8	13.0	12.5	12.5	13.4	13.1	12.6	106	1	1
$(HgTe)_{0.15}(InSb)_{0.85}$	10.2	10.1	9.4	10.3	9.6	9.3	9.9	9.8	10.2	9.7	110	1	1
InSb (polycr.)	4.0	3.2	2.9	3.1	3.2	3.0	3.1	3.6	3.2	3.2	142	6	4

scattering. This assumption gives for the Lorenz number the magnitude

$$L = 2(\frac{k}{e})^2 = 1.49 \times 10^{-8} \frac{W}{Ohm K^2} \qquad (3.7.2)$$

Calculations of κ_e on the basis of Eqns. (3.7.1), (3.7.2) and Table 8 gave the magnitudes of κ_e which are within the limits of the experimental error, and we may consider the data of Table 10 and Figure 21 as the lattice thermal conductivity.

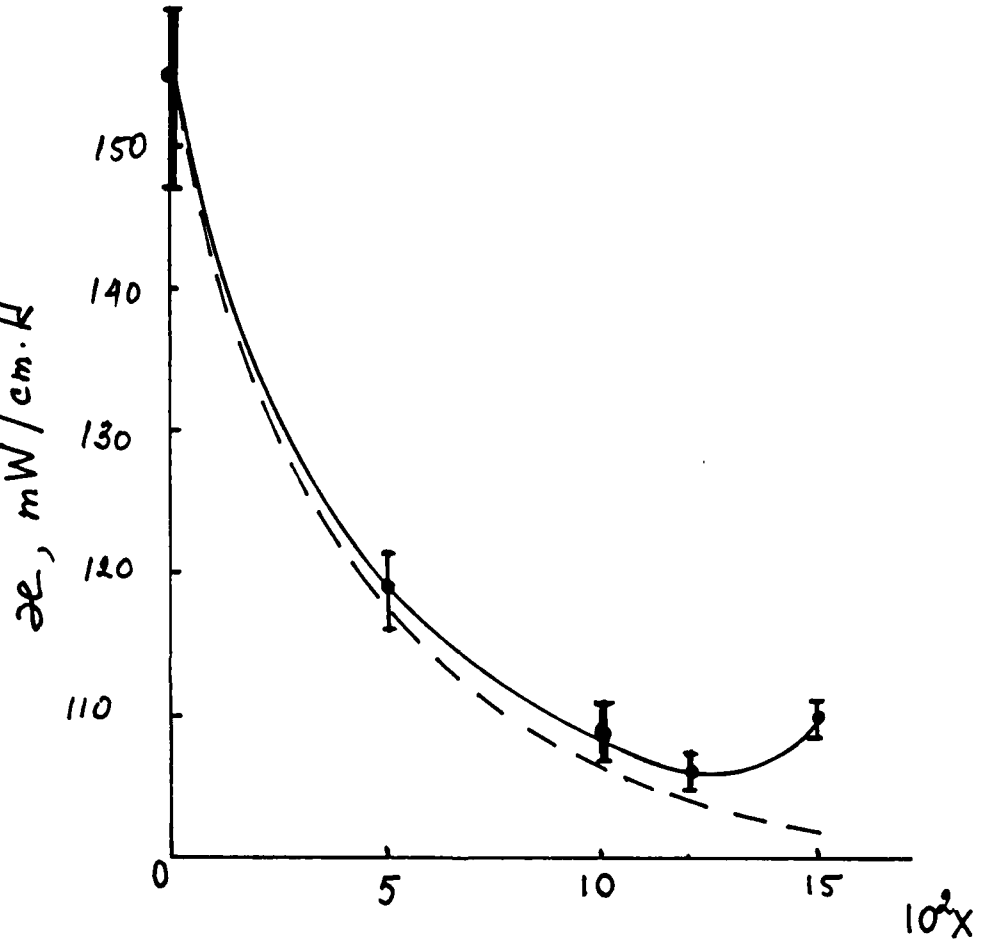

Figure 21. Thermal conductivity of the single crystals. The solid curve represents the experimental data, the dashed curve is the result of calculations on the basis of Abeles' model [39].

4. SUMMARY

The investigation of the problem of single crystal and epitaxial layer growth showed that the bulk crystals of the $(HgTe)_x(InSb)_{1-x}$ alloys might be grown with HgTe contents at least up to x = 0.15 by the conventional Bridgman-Stockbarger technique. Both hot-wall deposition, HWD, and evaporation-diffusion at the isothermal regime, EDRI, are effective for the epitaxial growth of the layers of HgTe on the InSb surface followed by the diffusion which will create an epilayer of a solid solution. It is important to mention that in the HgTe-InSb system, the usually existing composition gradient normal to the surface of the layer will not play as important a role as that which takes place in the systems like HgTe-CdTe or HgTe-ZnTe, because in these systems there is a strong dependence of the cut-off wavelength upon composition in contrast with HgTe-InSb.

The microstructure analysis and microhardness measurements showed that yield of the reproduceable quality single crystalline samples was high enough and that used regimes of synthesis of the crystals were reliable. During the reported year we had only one incident of ampule breakage which was caused by an internal defect in the fused silica used.

The microhardness measurements demonstrated that the grown crystals were highly uniform and the magnitude of this parameter was typical for single crystals.

The electrical, photoelectrical, and optical measurements showed the grown crystals had the transport and electro-optical

properties which are suitable for their use as a material for detection of the IR radiation.

Analysis of the experimental data and calculations on their basis have led us to conclude that the main goals of the second year of work on this project, namely

- development of methods of the single crystal and epitaxial layer growth,
- detailed structural and x-ray analysis of the grown crystals and films,
- evaluation of the principal electrical and galvanomagnetic properties,
- evaluation of the optical and photoelectric properties of the crystals and films and dependence of the properties on the growth parameters

have been achieved.

These results, coupled with the results of the first year of work, will be used in the next part of this project which consists mainly in manufacturing and investigation of the models of photo-resistive and photovoltaic infrared detectors on the basis of the new group of narrow-gap semiconductor materials: HgTe-InSb.

The achieved results have given us reason to believe that introduction of these materials in the infrared detection technique will help to improve some parameters of infrared detectors, such as uniformity of electro-optical properties, long-term stability, etc.

5. ACKNOWLEDGEMENTS

The authors, Dr. L. I. Berger and Dr. S. W. Lin, wish to thank Dr. L. J. Burnett, Chairman of the Physics Dept., Dr. S. B. W. Roeder, Chairman of the Chemistry Dept., Dr. R. Bedore, Chairman of the Mechanical Engineering Dept., and Dr. P. Kern, Chairman of the Geology Dept. of SDSU for the courteous opportunity to use department premises and equipment. We are grateful to Mr. R. Steed for his help in optical measurements.

We express our appreciation to Dr. A. Clawson of Naval Ocean Systems Center, San Diego, for the opportunity of verifying our results of galvano-magnetic measurements on the NOSC equipment. We thank Mr. Peter Gantzel of General Atomic Technology, Inc., San Diego, for the Laue X-ray analysis of some of our single crystals. We acknowledge the participation of Prof. Cesar Dias of the University of Baja California, Tijuana, Mexico, in the thermal conductivity measurements. We would like to express our thanks to Mrs. M. Oliver for typing the report.

We are especially grateful to the Office of Naval Research for the financial support which makes this investigation possible.

6. REFERENCES

1. C. E. Chang and W. R. Wilcox. J. Crystal Growth, 21, 135 (1974).
2. P. Capper, C. L. Jones, E. J. Pearce, and M. J. T. Quelch. J. Crystal Growth, 62, 487 (1983).
3. C. L. Jones, P. Capper, B. W. Straughan, and A. W. Vere. J. Crystal Growth, 63, 145 (1983).
4. P. Capper, J. J. G. Gosney, C. L. Jones, and M. J. T. Quelch. J. Crystal Growth, 63, 154 (1983).
5. W. A. Tiller. The Art and Science of Growing Crystals, J. Wiley, N.Y., 1963, p. 294.
6. L. I. Berger, S. W. Lin. "Quaternary Narrow-Band Semiconductors $(HgTe)_x(InSb)_{1-x}$ for Far-Infrared Detectors," 1984 Annual Report, Grant N00014-83-K-0588, ONR.
7. B. E. Bartlett, J. Deans, P. C. Ellen. J. Materials Sci., 4, 266 (1969).
8. Handbook of Chemistry and Physics, 64 Edition, CRC Press, 1983, p. E6.
9. V. M. Glazov, S. N. Chizhevskaya, and N. N. Glagoleva. Liquid Semiconductors, Nauka Publ. House, Moscow, 1967, p. 222 (in Russian).
10. A. Lopez-Otero. Thin Solid Films, 49, 3 (1978).
11. Y. Marfaing, G. Cohen-Solal, and F. Bailly. J. Phys. Chem. Solids Suppl., 1, 549 (1967).

12. J. Mumenberger, M. Sadeghi, E. Gruber, G. Elsinger, M. Sitter, and A. Lopez-Otero. J. Phys. C-5,43, C5-405 (1982).

13. K. Seeger. Semiconductor Physics, 3rd Edition. Springer-Verlag, Berlin, 1985, pp. 51, 59.

14. O. N. Tufte and E. L. Stelzer. J. Appl. Physics, 40, 4559 (1969).

15. G. Cohen-Solal, Y. Marfaing, F. Bailly, and M. Rodot. Compt. Rend., 261, 931 (1965).

16. G. Cohen-Solal, Y. Marfaing, and F. Bailly. Rev. Phys. Appl., 1, 11 (1966).

17. N. A. Gorunova, F. P. Kesamanly, D. N. Nasledov. "Phenomena in Solid Solutions," in Semiconductors and Semimetals, Acad. Press, N.Y. 4, 1968, p. 413.

18. I. V. Varlamov, L. A. Vyukov, F. I. Kozhokar, O. G. Maksimova, S. I. Radautsan, A. N. Solyakov, and V. N. Fillip. Inorg. Materials, 19, 156 (1983).

19. D. Brasen, J. Materials Sci. 11, 791 (1976); 13, 1776 (1978).

20. M. S. Abrahams, J. Blanc, and C. J. Buiocchi, Appl. Phys. Lett. 21, 185 (1972).

21. D. Laister and G. M. Jenkins. J. Materials Sci. 8, 1218 (1973).

22. M. Beoyens, J. S. Vermaak, and G. R. Proto. J. Appl. Phys. 49, 5435 (1978).

23. D. Y. Watts and A. F. W. Willoughby. Materials Lett., 2, 355 (1984).

24. D. Y. Watts and A. F. W. Willoughby. J. Appl. Phys., 56, 1869 (1984).

25. L. B. Valdes. Proc. IRE, 42, 420 (1954).

26. L. J. van der Pauw. Philips Res. Reps., 16, 187 (1961); 13, (1958); Philips Tech. Rev., 20, 220 (1958).

27. E. D. Palik and D. L. Mitchel, in Physics of Solids in Intense Magnetic Fields, Plenum Publ. Corp., 1969, p. 90.

28. F. Bassani and G. P. Parravicini. Electronic States and Optical Transitions in Solids, Pergamon Press, 1975.

29. L. I. Berger, L. I. Budilovich, and C. Z. Plotkina. "Non-destructive Quality Control," Proc. NIKIMP, 2(7), Moscow, 1972, p. 211 (in Russian).

30. T. Jasinski, W. M. Rohsenow, and A. F. Witt. J. Cryst. Growth, 61, 339 (1983).

31. C. A. Wang, A. F. Witt, and I. R. Carruthers. J. Cryst. Growth, 66, 299 (1984).

32. T. Jasinski and R. I. Naumann. J. Cryst. Growth, 66, 469 (1984).

33. P. Leroux-Hugon, Nguyen X. Xinh, and M. Rodot. J. Physique, 28, C1-73 (1967).

34. F. Kelemen, E. Cruceanu, and D. Niculescu. Phys. Status Solidi, 11, 865 (1965).

35. G. A. Slack. Phys. Rev. B, 6, 3791 (1972).

36. L. I. Berger. Ph.D. Diss. Moscow, 1959 (in Russian).

37. G. Leibfried, E. Schloman. Nachr. Akad. Wiss. Goettingen, Math Phys., 2a, 71 (1954).

38. R. W. Keyes. Phys. Rev., 115, 564 (1959).

39. B. Abeles. Phys. Rev., 131, 1906 (1963).

40. P. G. Klemens. Phys. Rev., 119, 507 (1960).

41. J. Callaway and H. C. von Baeyer. Phys. Rev., 120, 1149 (1960).

42. L. I. Berger, I. K. Shchukina, A. E. Balanevskaya. "Chim. Reagents α Preparates," Proc. IREA, 29, 246 (1966) (in Russian).

43. A. V. Ioffe and A. F. Ioffe. ZhTF, 28, 2357 (1958); (Soviet Physics--Tech. Phys., 3, p. 2163).

44. A. V. Ioffe. Soviet Physics-Solid State, 5, 3336 (1963).

45. F. R. Szofran and S. L. Lehoczky. Private communication.

46. R. J. Naumann and S. L. Lehoczky. J. Crystal Growth, 61, 707 (1983).

47. J. N. Zemel. J. Lumin., 7, 524 (1973).

48. P. Hansen. Constitution of Binary Alloys, McGraw-Hill, N.Y., 1958.

49. F. A. Shunk. Constitution of Binary Alloys, 2nd Supplement, McGraw-Hill, N.Y., 1969.

50. L. S. Palatnik, Y. F. Komnik, and V. M. Koshkin. Krystallografiya, 7, 563 (1962).

51. P. Becla, J. Lagowski, H. C. Gatos, and H. Ruda. (MIT). Private communication.

52. L. I. Alekseenko, B. F. Bilenky, Z. G. Grechukh, and V. G. Savitsky. Inorg. Materials, 10, 1215 (1974).

53. W. Bardsley and R. L. Bell. J. Electron. Contr., 3, 103 (1957).

54. J. D. Venables and R. M. Broudy. J. Appl. Phys., 29, 1025 (1958).

55. R. G. Rhodes. "Imperfections and Active Centers in Semiconductors," Pergamon Press, N.Y., 1964.

56. N. A. Goryunova, A. S. Borshchevsky, D. N. Tretiakov. In "Semiconductors and Semimetals." Physics of III-V Compounds, Vol. 4, Acad. Press, 1968.

57. M.S. Ablova and N. N. Feoktistova. Soviet Phys.-Solid State, 5, 265 (1963).

58. L. Svob, Y. Marfaing, R. Tribulet, F. Bailly, and G. Cohen-Solal. J. Appl. Phys., 46, 4251 (1975).

59. G. A. Antcliffe and H. Krauss. J. Phys. Chem. Solids, 30, 243, (1969).

60. S. H. Shin, M. Chu, A. H. B. Vanderwyck, M. Lanir, and C. C. Wang. J. Appl. Phys., 51, 3772 (1980).

61. S. M. Ryvkin. Photoelectric Effects in Semicondutors, Plenum Press, N.Y., 1964.

APPENDIX 1. DIMENSIONAL PARAMETERS OF THE TECHNOLOGICAL EQUIPMENT

1. Fused Silica Ampule Dimensions

1.1 Single crystal growth

Length: 20 to 23 cm

Outer diameter: 14 mm

Inner diameter: 10 mm

Silica rod: length 8 cm, diameter 9 mm

1.2. Synthesis

Length: 20 cm

Outer diameter: 19 mm

Inner diameter: 13.5 mm

Rod: length 8 cm, diameter 13 mm

2. Hot-Wall Epitaxial Growth Apparatus

2.1. Dimensions

Total height: 343 mm

Glass bell

- height: 25.4 cm
- outer diameter: 9.0 cm
- inside diameter: 8.4 cm

Stainless steel base dimensions

- height: 8 cm
- diameter: 11.5 cm

Radiation screen:

3 layers of aluminum foil, 20 cm height, 85 mm in diameter;

Heating elements

Substrate heater:

Silica tube

- length 6.6 cm
- outer diameter: 2.3 cm
- inner diameter: 1.9 cm

Heating element - Nichrom, gauge 24

- length 167 cm

Source holder and heater

Silica tube

- length: 95 mm
- outer diameter: 19.5 mm
- inner diameter: 13.5 mm

Heating element - Nichrom, gauge 24

- length 186 cm

2.2 Temperature regulation

- Thermocouples: chromel-alumel (Omega Engng, Inc.)
- Controllers: Omega, model 20A, Reostats;

Powerstat 3PN116C, Superior Electric Co.

3. Furnaces

3.1. Furnace for Single Crystal Growth

Dimensions: 23 cm long x 23 cm wide x 81 cm high

Outer quartz tube length = 48 cm, outside dia. = 3.6 m,
inside dia. = 3.0 cm

Inner quartz tube length = 27.3 cm, outside dia. = 2.9 cm,
inside dia. = 2.5 cm.

Upper brass tube length = 27.6 cm, outside diameter = 2.9 cm,
inside dia. = 2.4 cm

Heating elements:

Outer wiring (nichrome dia. = 0.02") length = 762 cm,
resistance $\approx$ 60 ohm

Inner wiring (nichrome dia. = 0.02") length = 457 cm,
resistance $\approx$ 35 ohm

Insulation material:

Insulating firebricks; 23 cm L x 11.5 cm W x 6.3 cm H
(Babcock and Wilcox)

Insulating fiberglass; 1 layer of a 15.8 cm thickness piece
(Owens Corning Fiberglass)

Temperature regulation:

Reostats: POWERSTAT 3PN116C, Superior Electric Co.

Power Supply: Harmonic Neutralized Constant Voltage Transformer 50LA, type CVS, Sola Electric Co.

Lowering mechanism:

Gorrel and Gorrel, type SM

3.2. Furnace for Synthesis

Dimensions: height = 38.7 cm, diameter = 27.6 cm

Quartz tube length = 37.8 cm, outside dia. = 3.6 cm, inside dia. = 2.93 cm

Copper tube length = 38.1 cm, outside dia. = 2.8 cm, inside dia. = 2.62 cm

Heating element:

Nichrome wire gauge 24, length = 670 cm, resistance = 35 ohm

Insulating material:

Insulating firebricks (Babcock and Wilcox)

Temperature regulation:

Temperature controller OMEGA, model 20M, OMEGA Engineering Inc.

3.3. Annealing Furnace

Dimensions:

outside 31.0 cm L x 33.5 cm W x 30.0 cm H

inside 11.5 cm L x 20.0 cm W x 19.5 cm H

Heating element:

Nichrome wire dia. = .4", length = 1550 cm, resistance = 21 ohm

Insulating material:

Insulating Firebricks (Babcock and Wilcox)

Temperature regulation:

Temperature controller OMEGA, model 20M, OMEGA Engineering Inc.

APPENDIX 2. INFLUENCE OF THE DETECTOR ACTIVE ELEMENT THICKNESS ON MAGNITUDE OF THE OUTPUT SIGNAL

The optimal thickness, l_o, of a photoresistor from Lambert-Bouquer's law:

$$l_o = (\ln J_o/J)/k \qquad \text{(A2-1)}$$

where k is the absorption coefficient and J_o/J is a portion of the initial radiation absorbed by the layer l_o. We may consider, for example, $J_o/J = 100$. Thus

$$l_o = 4.65/k \qquad \text{(A2-2)}$$

For InSb at 77K, $k \approx 10^3 cm^{-1}$ and $l_o \approx 10$ μm. Such a thickness is technologically difficult to achieve and usually thickness $l > l_o$ (Figure A2-1). Let us consider the influence of the "excessive" thickness on magnitude of the output signal.

If $l/l_o = n$, the total resistance may be written as

$$R_D = R_o/n. \qquad \text{(A2-3)}$$

if the detector is not illuminated. Resistance of the illuminated detector, R_L, is

$$R_L = \left[\frac{1}{R_o - \Delta R_o} + \frac{n-1}{R_o}\right]^{-1}$$

or

$$R_L = \frac{(R_o - \Delta R_o)}{nR_o - \Delta R(n-1)} \qquad \text{(A2-4)}$$

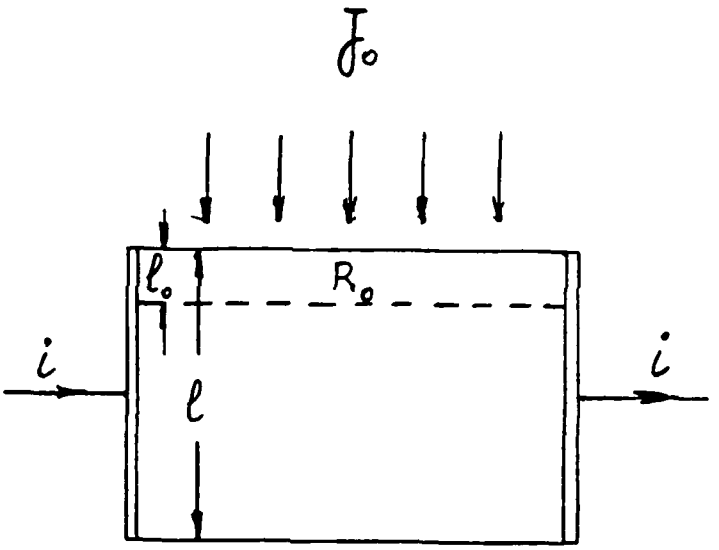

Figure A2-1.

Combining Eqns. (A2-3) and (A2-4) yields

$$\Delta R = R_D - R_L = \frac{R_o \cdot \Delta R_o}{n^2 R_o - n\Delta R_o (n-1)} \qquad \text{(A2-5)}$$

The relative change of the detector resistivity

$$\Delta R/\Delta R_o = R_o/[n^2 R_o - \Delta R_o (n-1)n] \qquad \text{(A2-6)}$$

The ratio $\Delta R / \Delta R$ shows attenuation of the output signal caused by the "ballast" thickness of the detector active element. Denoting $\Delta R_o/\Delta R = a$ (the attenuation coefficient), we can rewrite (A2-6) in the form

$$a = n^2 - n(n-1)\Delta R_o/R_o$$

or

$$a = \left(\frac{l}{l_o}\right)^2 - \frac{l}{l_o}\left(\frac{l}{l_o} - 1\right) \Delta R_o/R_o \qquad \text{(A2-7)}$$

For an n-type material

$$a = \left(\frac{l}{l_o}\right)^2 - \frac{l}{l_o}\left(\frac{l}{l_o} - 1\right) \frac{\Delta p}{p_o + \Delta p} \qquad \text{(A2-8)}$$

where p is the minority charge concentration.

In this consideration we assume that $l \geq l_o$, and l_o is chosen from the condition

$$J \ll J_o \qquad \text{(A2-9)}$$

AD-A166 008 QUATERNARY NARROW-BAND SEMICONDUCTORS (HGTE)X(INSB)1-X FOR FAR-INFRARED DETECTORS(U) SAN DIEGO STATE UNIV FOUNDATION CA L I BERGER 31 AUG 86 N00014-83-K-0588 2/2

UNCLASSIFIED F/G 17/5 NL

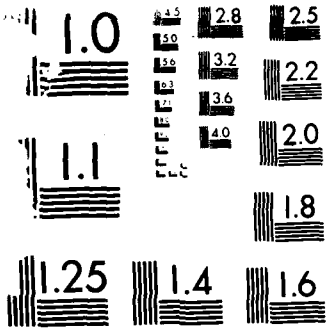

MICROCOPY RESOLUTION TEST CHART

STANDARDS 1963 A

The condition (A2-9) is followed by the conclusion that photoconductivity of the element does not depend on the absorption coefficient [61] and depends only on J_o. One can see that the analysis of total efficiency of a photoresistive detector has to include combined photoelectric and geometrical consideration.

END

DTIC

4-86